NON-LINEAR SPATIAL MULTIGRID METHOD FOR NON-LINEAR S_2 ACCELERATION

A Thesis

by

JOHN DAVID KLIEWER

Submitted to the Office of Graduate and Professional Studies of
Texas A&M University
in partial fulfillment of the requirements for the degree of

MASTER OF SCIENCE

Chair of Committee,	Jim E. Morel
Committee Members,	Jean C. Ragusa
	Bojan Popov
Head of Department,	Yassin A. Hassan

May 2018

Major Subject: Nuclear Engineering

ABSTRACT

A nonlinear spatial multigrid algorithm was developed and explored as a technique to efficiently solve the nonlinear S_2 acceleration equations for S_N neutron transport calculations in 1-D slabs. Acceleration of the basic source iteration process in S_N calculations is necessary in problems with highly diffusive regions. Direct inversion would be a more efficient method in 1-D, but a multigrid method has the potential to be far more efficient than other techniques in 2-D. This work is a first step toward a 2-D multigrid algorithm. The computational results show that this scheme works well for optically-thin cells on the fine mesh, but degrades significantly for optically-thick cells on the fine mesh.

CONTRIBUTORS AND FUNDING SOURCES

Contributors

This work was supported by a thesis committee consisting of Professor Jim E. Morel, advisor, and Jean C. Ragusa, both of the Department of Nuclear Engineering, and Professor Bojan Popov of the Department of Mathematics.

All other work conducted for the thesis was completed by the student independently.

Funding Sources

Graduate study was supported by a graduate research assistantship from Texas A&M University with funding from the Center for Exascale Radiation Transport (CERT), in turn funded through the Predictive Science Academic Alliance Program (PSAAP) of the National Nuclear Security Administration (NNSA).

NOMENCLATURE

x	Position (cm)
x_{min}	Minimum value of x in the problem. (cm)
x_{max}	Maximum value of x in the problem. (cm)
h	Cell width. (cm)
$\sigma_t(x)$	Macroscopic total cross section $(1/\text{cm})$
$\sigma_s(x)$	Macroscopic scattering cross section $(1/\text{cm})$
c	Scattering ratio
$q(x)$	Independent source $\left(\frac{\text{neutrons}}{\text{cm}^3\ \text{s}}\right)$
μ	Directional cosine
μ_m	Discretized directional cosine
ℓ	Multigrid iteration index
$\jmath$	Source iteration index
$\psi(\mu, x)$	Angular flux $\left(\frac{\text{neutrons}}{\text{biradian cm}^2\ \text{s}}\right)$
$\tilde{\psi}(\mu_m, x)$	Angular flux (LD approximation) $\left(\frac{\text{neutrons}}{\text{biradian cm}^2\ \text{s}}\right)$
$\phi^{\pm}(x)$	Half-range scalar flux $\left(\frac{\text{neutrons}}{\text{cm}^2\ \text{s}}\right)$
$\tilde{\phi}^{\pm}(x)$	Half-range scalar flux (LD approximation) $\left(\frac{\text{neutrons}}{\text{cm}^2\ \text{s}}\right)$
$\langle \mu_i^{\pm} \rangle$	μ-average
$\phi(x)$	Scalar Flux $\left(\frac{\text{neutrons}}{\text{cm}^2\ \text{s}}\right)$
$\tilde{\phi}(x)$	Scalar Flux (LD approximation) $\left(\frac{\text{neutrons}}{\text{cm}^2\ \text{s}}\right)$
EAS	Exact analytic solution
ICS	Iteratively converged solution

TABLE OF CONTENTS

Page

LIST OF FIGURES

FIGURE Page

LIST OF TABLES

TABLE Page

1. INTRODUCTION AND LITERATURE REVIEW

1.1 Basic Concepts

Neutron transport is an important area of research in computational physics and is of paramount importance in applications such as nuclear reactor design and shielding. Scalar flux (ϕ) is of particular importance for determining neutron interaction rates.

Transport problems do not have analytic solutions in most real-world applications, so the transport analyst must turn to numerical techniques. A solution algorithm is paired with a discretization scheme and applied to a transport problem (with its physical parameters and boundary conditions). In this thesis, the spatial discretization scheme is linear-discontinuous (LD) Galerkin, and the angular discretization is in S_N discrete ordinates. Successive iterates converge to a discrete solution defined by the discretization scheme. The approximation to which the iterates converge is termed the *iteratively converged solution* (ICS).

1.2 The Boltzmann Equation

Neutron transport can be characterized quantitatively with the Boltzmann equation, which is a particle balance equation in 7-D phase space.

One generalized version of the Boltzmann equation for neutron transport is[1]

$$\begin{aligned} & \frac{1}{v}\frac{\partial\psi}{\partial t} + \vec{\Omega}\cdot\nabla\psi + \sigma_t(\vec{r},E)\psi(\vec{r},E,\vec{\Omega},t) \\ = & \int_{4\pi}\int_0^\infty \sigma_s(\vec{r},E'\rightarrow E,\vec{\Omega}'\rightarrow\vec{\Omega})\,\psi(\vec{r},E',\vec{\Omega}',t)\,dE'\,d\Omega' \\ + & \frac{\chi(E)}{4\pi}\int_{4\pi}\int_0^\infty \nu(E')\sigma_f(\vec{r},E')\,\psi(\vec{r},E',\vec{\Omega}',t)\,dE'\,d\Omega' + q(\vec{r},E',\vec{\Omega}',t). \end{aligned} \tag{1.1}$$

The quantities appearing in the Boltzmann equation are described in Table 1.1. The unit vector $\vec{\Omega}$ denotes the direction of flight of a neutron in 3-D space. See Fig. 1.1. The polar angle θ has been defined in reference to the x axis.

Symbol	Units	Name	Comments
$\psi(\vec{r}, E, \vec{\Omega}, t)$	$\frac{\text{neutrons}}{\text{cm}^2 \text{ sr eV } s}$	Angular Flux	
$\sigma_t(\vec{r}, E)$	$\frac{1}{\text{cm eV}}$	Total macroscopic cross section	
$\sigma_f(\vec{r}, E')$	$\frac{1}{\text{cm eV}}$	Fission macroscopic cross section	
$\sigma_s(\vec{r}, E' \to E, \vec{\Omega}' \to \vec{\Omega})$	$\frac{1}{\text{cm sr eV}}$	Scattering macroscopic cross section	$\sigma_s \, dE \, d\Omega$ represents the macroscopic cross section for scattering a neutron with initial energy E' and initial direction Ω' into direction $d\Omega$ about $\vec{\Omega}$ with energy dE about E.
E	eV	Neutron energy	
v	$\frac{\text{cm}}{\text{s}}$	Neutron speed	Speed is a function of energy
$\vec{\Omega}$		Neutron direction	Unit vector indicating direction of particle flight
t	s	Time	Point in time (not time interval)
$d\Omega$	sr	Differential solid angle	
$\chi(E)$	$\frac{1}{\text{eV}}$	Fission spectrum	
$\nu(E)$			Average number of neutrons released per fission
$q(\vec{r}, E', \vec{\Omega}', t)$	$\frac{\text{neutrons}}{\text{cm}^3 \text{ sr eV } s}$	Independent source	Volumetric, flux-independent neutron source.

Table 1.1: Variables appearing in the Boltzmann Equation (Eqn. 1.1).

Each term in Eqn. 1.1 has a physical meaning. Let

$$dP = dV dE d\Omega, \tag{1.2}$$

where dP is the differential phase space volume and dV, dE, and $d\Omega$ are the differential volume, energy, and direction, respectively. Because time-dependent behavior is not examined in this thesis, dt is omitted from Eqn. 1.2.

The expression $\frac{1}{v}\frac{\partial \psi}{\partial t} dP$ represents the time rate of change of the number of neutrons in dP. The speed v is a function of E. The meaning of this term becomes more obvious by considering

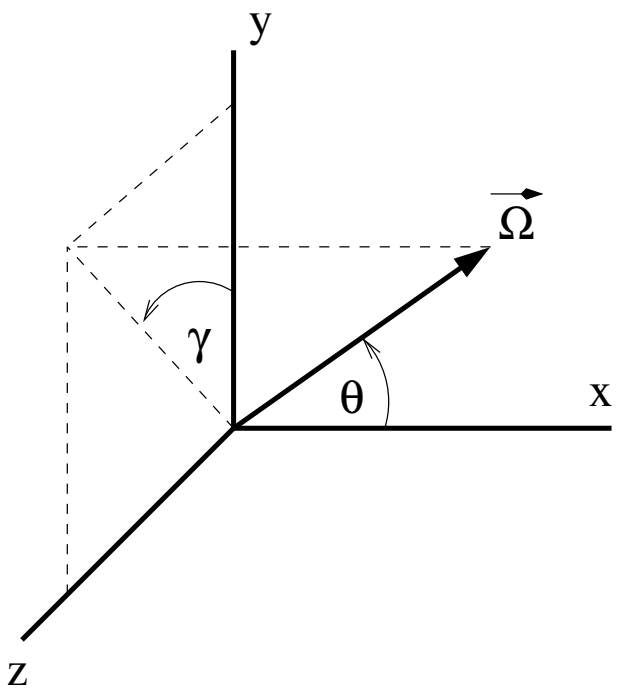

Figure 1.1: Cartesian coordinate system with direction vector and angles. $|\vec{\Omega}| = 1$.

the relation between ψ and the neutron density n, $n = \frac{\psi}{v}$, where $n\,dP$ represents the number of neutrons in dP.

The leakage term $\vec{\Omega} \cdot \nabla\psi\,dP$ represents the net rate at which neutrons exit dP by crossing the surface of dV. Consider a volume V_0 bounded by a surface S_0. Then, by applying Gauss' Law, $\int_{V_0} \vec{\Omega} \cdot \nabla\psi\,dV = \oint_{S_0} \psi\vec{\Omega} \cdot \vec{n}\,dA$, where $\vec{n}$ is the unit vector normal to differential surface dA of surface S_0, pointing outside of volume V_0. The expression $\oint_{S_0} \psi\vec{\Omega} \cdot \vec{n}\,dA\,dE\,d\Omega$ more clearly represents the net neutron flow out of V_0 through S_0 in dE about E and $d\Omega$ about $\vec{\Omega}$. However, since the other terms of Eqn. 1.1 are expressed as volumetric quantities, it is necessary to express the leakage term as a volume-integrable quantity rather than as a surface-integrable quantity.

The term $\sigma_t\psi\,dP$ represents the number of neutrons interacting in dP. Each interaction can be classified as either an absorption or a scattering event. An absorption removes a neutron from volume dV. A scattering event changes E and $\vec{\Omega}$, removing the neutron from the energy range dE' about E' and the direction range $d\Omega'$ about $\vec{\Omega}'$.

The inscattering term $\left[\int_{4\pi}\int_0^\infty \sigma_s\psi\,dE'\,d\Omega'\right] dP$ represents the rate at which neutrons are scat-

tered into dE about E and $d\Omega$ about $\vec{\Omega}$.

The fission source term $\left[\frac{\chi(E)}{4\pi}\int_{4\pi}\int_0^\infty \nu\sigma_f\psi\, dE'd\Omega'\right] dP$ represents the rate at which neutrons are created in dP by neutron-induced fission. On average, ν neutrons are released per fission. The inner integral gives the volumetric rate of neutron production from induced fission per steradian. The outer integral integrates over the unit sphere to compute the volumetric neutron production rate over all directions. Treating fission as an isotropic phenomenon, the outer integral is divided by 4π steradians, which is then multiplied by $\chi(E)$. The fission spectrum function $\chi(E)$ is normalized so that $\int_0^\infty \chi(E)\, dE = 1$. The average number of fission neutrons in dE per fission neutron is $\chi(E)dE$.

The independent source term $q\, dP$ represents the rate at which neutrons in dP are created in volume dV about $\vec{r}$, independent of ψ.

Equation 1.1 does not account for delayed fission neutrons, but this point is moot since we consider only subcritical source problems in this thesis. Solving this generalized equation for a real-world problem is exceedingly difficult.

1.3 The Transport Equation

The transport equation to be solved in this thesis is given by

$$\mu\frac{\partial\psi}{\partial x}(\mu,x)+\sigma_t(x)\psi(\mu,x)=\frac{\sigma_s(x)}{2}\phi(x)+\frac{q(x)}{2}\quad\forall x\in[x_{\min},x_{\max}]\text{ and }\mu\in[-1,1]. \tag{1.3}$$

The meanings of quantities given in Eqn. 1.3 are given in Table 1.2.

1.3.1 Convention for ψ with 1-D Angular Component

Up to this point, ψ has been expressed in terms of solid angle, as the foregoing discussion was for the Boltzmann equation in three spatial dimensions. In transitioning to 1-D space, ψ can also be expressed in terms of another parameter, μ, analogous to polar angle θ. To visualize the meaning of μ, one can think of a right circular cone, with the apex on the x axis, which is collinear with the axis of the cone. For a given μ, $\theta = \arccos\mu$, where θ is the angle between the lateral surface and axis of the cone. See Fig. 1.2.

Symbol	Units	Name	Comments
$\psi(\mu, x)$	$\frac{\text{neutrons}}{\text{cm}^2 \text{ biradian } s}$	Angular Flux	
$\sigma_t(x)$	$\frac{1}{\text{cm}}$	Total macroscopic cross section	
$\sigma_s(x)$	$\frac{1}{\text{cm}}$	Scattering macroscopic cross section	
μ	biradian	Neutron direction	$\mu = \cos\theta$
$q(x)$	$\frac{\text{neutrons}}{\text{cm}^3 \text{ s}}$	Independent source	Volumetric, flux-independent neutron source.

Table 1.2: Variables appearing in the 1-D transport equation (Eqn. 1.3).

In the 1-D transport equation (Eqn. 1.3), ψ is dependent upon θ via μ but independent of azimuth angle.

The unit sphere is the set of all possible endpoints for $\vec{\Omega}$. Accordingly, $d\Omega = dA$. In Fig. 1.3, the differential area $d\Omega$ forms a "ribbon" of circumference $2\pi \sin\theta$ and width $d\theta$, so that

$$d\Omega = (2\pi \sin\theta) d\theta. \tag{1.4}$$

If $\mu = \cos\theta$, then $\frac{d\mu}{d\theta} = \sin\theta$, and

$$\begin{aligned} d\Omega &= 2\pi(\sin\theta)d\theta \\ &= 2\pi \frac{d\mu}{d\theta} d\theta \\ &= 2\pi d\mu. \end{aligned} \tag{1.5}$$

For a unit circle,

$$\int_{4\pi} d\Omega = 2\pi \int_{-1}^{1} d\mu = 4\pi \text{ steradians}, \tag{1.6}$$

as one would expect. The key concept here is that $d\Omega = \text{constant} \cdot d\mu$. Seeing that $\frac{d\Omega}{d\mu}$ is constant over the entire range of solid angle, one can elect to express ψ in units for μ rather than for $\vec{\Omega}$. Since the full span of μ is 2, μ is essentially a "per hemisphere" unit of solid angle. The term *biradian* is herein used to refer to this "per hemisphere" unit for μ.

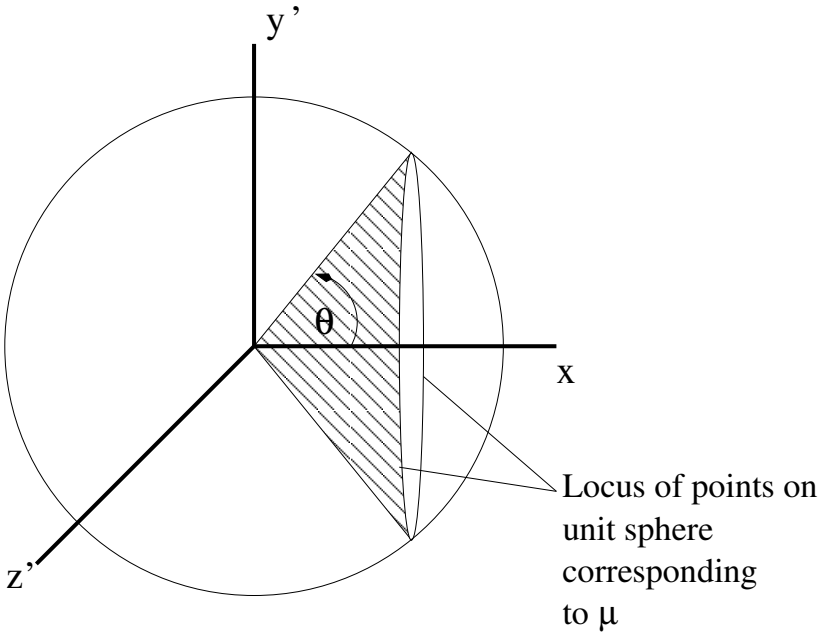

Figure 1.2: Directional cone for $\mu = \cos\theta$.

Hence, rather than expressing scalar flux ϕ as

$$\phi = \int_{4\pi} \psi \, d\Omega = 2\pi \int_{-1}^{1} \psi \, d\mu \;\; (\psi \text{ expressed using steradians}), \tag{1.7}$$

the following relation is used to compute ϕ from ψ:

$$\phi = \int_{-1}^{1} \psi \, d\mu \;\; (\psi \text{ expressed using biradians}). \tag{1.8}$$

1.3.2 Transport Equation Assumptions

The following simplifying assumptions are made:

1. Spatial variable is 1-D.

2. Problem is steady-state (independent of time).

3. No neutron multiplication (fission).

4. No energy dependence. This is can be thought of as a single energy group problem, but our

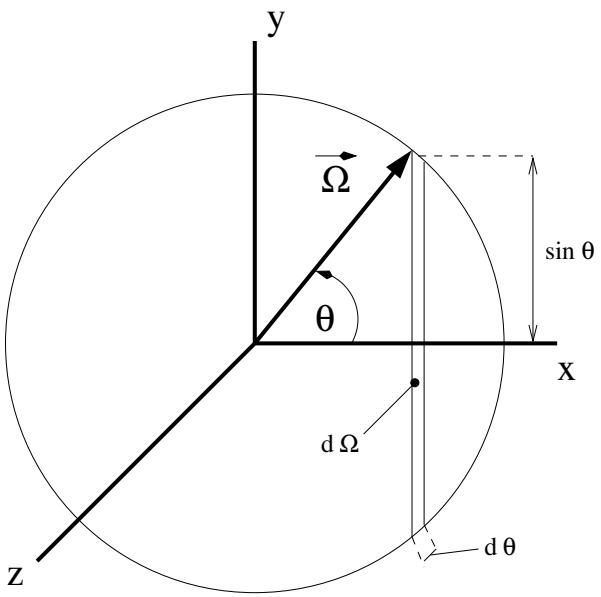

Figure 1.3: Unit sphere and μ.

method can be applied to the energy-dependent case via the multigroup method.[2] For the sake of brevity, we will not further discuss this.

5. Scattering is isotropic in the lab frame. Our method can easily accommodate anisotropic scattering[3], but for the sake of brevity, we will not discuss this further.

Boundary conditions in the spatial domain are vacuum, prescribed source, or specularly reflective. Source conditions are

$$\psi(\mu, x_{\min}) = \psi_{L,\text{in}}(\mu) \quad \forall \mu \in (0, 1] \tag{1.9}$$

for the left boundary and

$$\psi(\mu, x_{\max}) = \psi_{R,\text{in}}(\mu) \quad \forall \mu \in [-1, 0) \tag{1.10}$$

for the right boundary. Vacuum conditions for each boundary are set by setting the respective source conditions to zero. Reflective conditions are given by

$$\psi(\mu, x_{\min}) = \psi(-\mu, x_{\min}) \quad \forall \mu \in (0, 1] \tag{1.11}$$

for the left boundary and

$$\psi(\mu, x_{\max}) = \psi(-\mu, x_{\max}) \quad \forall \mu \in [-1, 0) \tag{1.12}$$

for the right boundary.

1.4 Source Iteration

Source iteration (SI) is the simplest numerical solution technique for transport problems which is guaranteed to converge in non-multiplying problems in which $\sigma_s < \sigma_t$, or $\sigma_s \leq \sigma_t$ if the problem is spatially bounded.[3]

Consider Eqn. 1.3 in a more concise form:

$$\mu \frac{\partial \psi}{\partial x} + \sigma_t \psi = \frac{\sigma_s}{2} \phi + \frac{q}{2}. \tag{1.13}$$

The abstract operator form of transport equation Eqn. 1.13 is given by

$$L\psi = \underbrace{S\psi + q}_{\text{Source Term } Q}, \tag{1.14}$$

where transport operator

$$L = \mu \frac{\partial}{\partial x} + \sigma_t \tag{1.15}$$

and scattering operator

$$S = \frac{1}{2} \int_{-1}^{1} \sigma_s(\cdot)\, d\mu'. \tag{1.16}$$

For the purpose of enumerating source iterations, let $\jmath$ begin at $\jmath = 0$. In operator form, source iteration is expressed as

$$L\psi^{(\jmath+1)} = S\psi^{(\jmath)} + \frac{q}{2}. \tag{1.17}$$

Applied to the transport equation (Eqn. 1.13), the source iteration equation becomes

$$\mu\frac{\partial\psi^{(\jmath+1)}}{\partial x}+\sigma_t\psi^{(\jmath+1)}=\frac{\sigma_s}{2}\phi^{(\jmath)}+\frac{q}{2}. \tag{1.18}$$

The index $\jmath$ denotes the approximation from the $\jmath$-th generation, where the index $\jmath=0$ in $\phi^{(0)}$ represents the initial guess for ϕ. Eqn. 1.18 is used to solve for $\psi^{(\jmath+1)}$. The approximation for ϕ is updated by computing $\phi^{(\jmath+1)}=\int_{-1}^{1}\psi^{(\jmath+1)}\,d\mu$. If consecutive source iterations are to be performed, $\jmath$ is incremented by one, and the updated $\phi^{(\jmath)}$ is then substituted into Eqn. 1.18 to solve for the next iterate for ψ, $\psi^{(\jmath+1)}$. This process is repeated until the solution for ψ is deemed to be sufficiently converged.

1.4.1 Physical Meaning of Source Iterations

Consider Eqn. 1.17. Assuming a zero initial guess, $\psi^{(0)}\equiv 0$, there is no scattering in the first iteration ($\jmath=0$). Thus, the solution $\psi^{(1)}$ for the initial iteration must be uncollided flux, with contributions from the independent source q and source boundary conditions only. The second iteration takes $\psi^{(1)}$ as the input for the scattering source. There is still uncollided flux because of q and/or the boundary source. However, now there is the contribution of scattered flux, all of which was produced in the first iteration and so has been scattered once. The solution $\psi^{(2)}$ of the second iteration is composed exclusively of uncollided and once-scattered flux. The solution $\psi^{(3)}$ for the third iteration includes a scattered-flux component from the $\psi^{(2)}$ from the previous iteration, thus incrementing the maximum possible number of scattering events for a given neutron by one, for at most two scattering events. Thus, it is seen that, starting from a zero guess, any neutron in $\psi^{(\jmath)}$ has been scattered at most $\jmath-1$ times.

The relationship between iteration count and maximum possible number of scattering interactions for any particle provides qualitative insight into why SI is slow to converge for $c\to 1$ in optically-thick media. In evaluating $\psi^{(\jmath)}$, the S term can vary, while the q term is constant. Therefore, in an infinite medium, any change between $\psi^{(\jmath-1)}$ and $\psi^{(\jmath)}$ is effected only by the S term. The component of the flux which survives into the next generation/iteration $\psi^{(\jmath)}$ is $c\psi^{(\jmath-1)}$.

By extension, the component of flux from past generation $\imath$ surviving into current generation $\jmath$ is $c^{\jmath-\imath}\psi^{(\imath)}$. It is readily apparent that past iteration components of $\psi^{(\jmath)}$ quickly die out for small c but have an increasing propensity to linger as $c \to 1$, which inhibits convergence.

Slowly converging problems present two challenges. First, SI becomes inefficient for these problems, and it becomes desirable to apply techniques to accelerate their convergence. Another, more subtle issue is that slow convergence complicates the test for convergence.

1.5 Spatial Discretization Scheme

An LD Galerkin spatial discretization scheme is used to test the acceleration technique. The LD Galerkin scheme is piecewise linear-discontinuous and exhibits better stability than the diamond scheme. Within cell i, the spatial discretization scheme for ψ_m is linear-discontinuous, defined by a linear combination of two *trial space* functions,

$$\tilde{\psi}_{m,i}(x) = \frac{x_{i,R} - x}{h_i}\psi_{m,i,L} + \frac{x - x_{i,L}}{h_i}\psi_{m,i,R}, \tag{1.19}$$

where $\psi_{m,i,L}$ and $\psi_{m,i,R}$ are the parameters which define the LD solution $\tilde{\psi}_m$ in cell i, $x = x_{i,L}$ at the left cell i edge, $x = x_{i,R}$ at the right cell i edge, and $h_i = x_{i,R} - x_{i,L}$ is the width of cell i.

Allowing $\tilde{\psi}$ to be discontinuous at cell edges requires a method of assigning values of the solution on the edges. Here, *upwinding* is applied to resolve this ambiguity. That is, for a given μ, the incoming flux (the flux on the edge) is taken to be the flux just inside the edge of the cell from which the flux is about to flow across the edge. For cell i:

$$\tilde{\psi}_m(x_{i,L}) = \psi_{m,i-1,R} \quad \forall \mu_m > 0 \tag{1.20}$$

$$\tilde{\psi}_m(x_{i,L}) = \psi_{m,i,L} \quad \forall \mu_m < 0 \tag{1.21}$$

$$\tilde{\psi}_m(x_{i,R}) = \psi_{m,i,R} \quad \forall \mu_m > 0 \tag{1.22}$$

$$\tilde{\psi}_m(x_{i,R}) = \psi_{m,i+1,L} \quad \forall \mu_m < 0 \tag{1.23}$$

For $\mu > 0$, the edge flux is taken from the ψ_R in the left cell. For $\mu < 0$, the edge flux is taken from the ψ_L in the right cell. Upwinding applies to $\tilde{\phi}^+$ ($\mu > 0$) and $\tilde{\phi}^-$ ($\mu < 0$) as well. See Figs. 1.4 and 1.5.

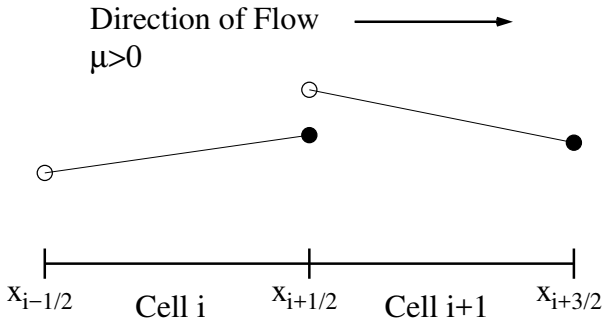

Figure 1.4: LD upwinding for ψ with $\mu > 0$ and ϕ^+.

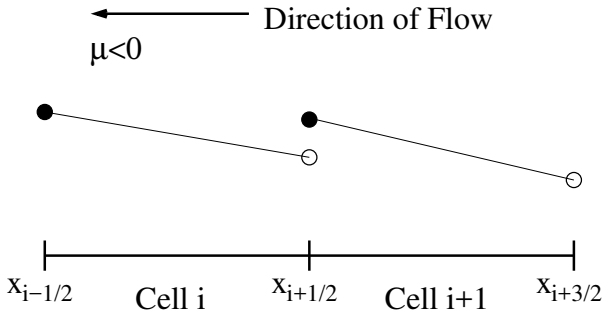

Figure 1.5: LD upwinding for ψ with $\mu < 0$ and ϕ^-.

Spatial moment equations are formed to solve for $\tilde{\psi}_m$. In addition to the trial space defined in Eqn. 1.19, the notion of a complementary *weight space* comes into play here. For a particular cell in a particular grid, the weight space is spanned by the weight functions given in Eqns. 1.24 and 1.25. As is evident from comparing Eqns. 1.24 and 1.25 with Eqn. 1.19, these are the basis functions on the trial space on the finest grid as well. Unlike the weight space, the trial space does not retain this form on coarser grids.

The two cell-wise spatial moment equations for $\tilde{\psi}_m$ are formed by first substituting $\tilde{\psi}_{m,i}(x)$ from Eqn. 1.19 for $\psi_m^{(j+1)}$, the constant cell-wise values for σ_t and σ_s, and the cell-wise linear function $q(x)$ into Eqn. 1.33. The resulting equation is then multiplied by a weight function and integrated over the cell width h_i. The weight functions used in this analysis and depicted in Fig. 1.6, are

$$W_{i,L}(x) = \frac{x_{i,R} - x}{h_i},\ x \in [x_{i,L}, x_{i,R}] \tag{1.24}$$

and

$$W_{i,R}(x) = \frac{x - x_{i,L}}{h_i},\ x \in [x_{i,L}, x_{i,R}]. \tag{1.25}$$

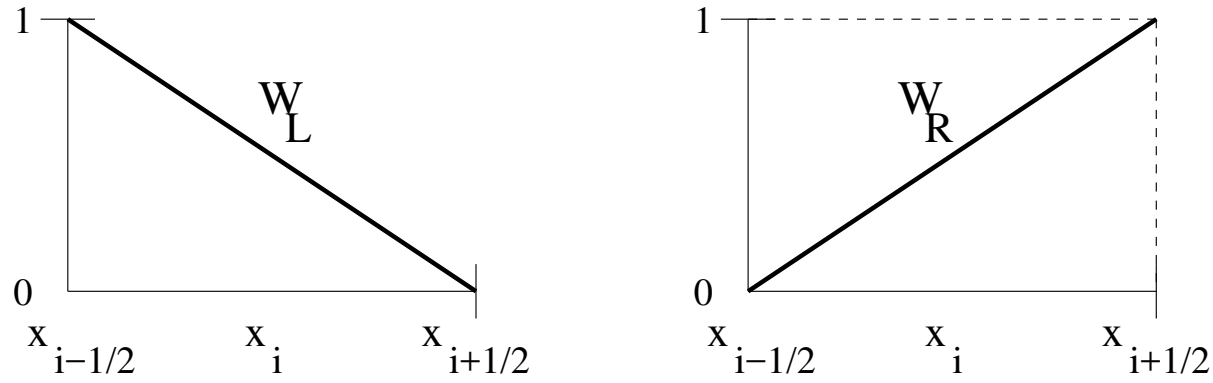

Figure 1.6: Weight functions on cell i.

In order to account for upwinding, for each basis function, two different versions of the moment equation are derived, one in which $\mu_m > 0$ and one in which $\mu_m < 0$.

1.5.1 S_N Moment Equations for $\mu_m > 0$

For weight function W_L

$$\begin{aligned} &\frac{\mu_m}{2}\left(\psi_{m,i,L}^{(j+1)} + \psi_{m,i,R}^{(j+1)}\right) + \frac{\sigma_{t,i}h_i}{2}\left(\frac{2}{3}\psi_{m,i,L}^{(j+1)} + \frac{1}{3}\psi_{m,i,R}^{(j+1)}\right) \\ &= \frac{\sigma_{s,i}h_i}{2}\left(\frac{1}{3}\phi_{i,L}^{(j)} + \frac{1}{6}\phi_{i,R}^{(j)}\right) + \frac{h_i}{2}\left(\frac{1}{3}q_{i,L} + \frac{1}{6}q_{i,R}\right) + \mu_m\psi_{m,i-1,R}^{(j+1)}. \end{aligned} \tag{1.26}$$

For weight function W_R

$$\frac{\mu_m}{2}\left(\psi^{(j+1)}_{m,i,R}-\psi^{(j+1)}_{m,i,L}\right)+\frac{\sigma_{t,i}h_i}{2}\left(\frac{1}{3}\psi^{(j+1)}_{m,i,L}+\frac{2}{3}\psi^{(j+1)}_{m,i,R}\right)$$
$$=\frac{\sigma_{s,i}h_i}{2}\left(\frac{1}{6}\phi^{(j)}_{i,L}+\frac{1}{3}\phi^{(j)}_{i,R}\right)+\frac{h_i}{2}\left(\frac{1}{6}q_{i,L}+\frac{1}{3}q_{i,R}\right). \tag{1.27}$$

1.5.2 S_N Moment Equations for $\mu_m < 0$

For weight function W_L

$$\frac{\mu_m}{2}\left(\psi^{(j+1)}_{m,i,R}-\psi^{(j+1)}_{m,i,L}\right)+\frac{\sigma_{t,i}h_i}{2}\left(\frac{2}{3}\psi^{(j+1)}_{m,i,L}+\frac{1}{3}\psi^{(j+1)}_{m,i,R}\right)$$
$$=\frac{\sigma_{s,i}h_i}{2}\left(\frac{1}{3}\phi^{(j)}_{i,L}+\frac{1}{6}\phi^{(j)}_{i,R}\right)+\frac{h_i}{2}\left(\frac{1}{3}q_{i,L}+\frac{1}{6}q_{i,R}\right). \tag{1.28}$$

For weight function W_R

$$-\frac{\mu_m}{2}\left(\psi^{(j+1)}_{m,i,L}+\psi^{(j+1)}_{m,i,R}\right)+\frac{\sigma_{t,i}h_i}{2}\left(\frac{1}{3}\psi^{(j+1)}_{m,i,L}+\frac{2}{3}\psi^{(j+1)}_{m,i,R}\right)$$
$$=\frac{\sigma_{s,i}h_i}{2}\left(\frac{1}{6}\phi^{(j)}_{i,L}+\frac{1}{3}\phi^{(j)}_{i,R}\right)+\frac{h_i}{2}\left(\frac{1}{6}q_{i,L}+\frac{1}{3}q_{i,R}\right)-\mu_m\psi^{(j+1)}_{m,i+1,L}. \tag{1.29}$$

A complete derivation of the S_N moment equations is given in Appendix A.

1.6 Source Iteration on S_N Moment Equations

For each sweep in $\mu_m > 0$, Eqns. 1.26 and 1.27 are solved as 2×2 system, sequentially by cell, starting at the left end. In cell i, this system of two equations is solved for $\psi^{(j+1)}_{m,i,L}$ and $\psi^{(j+1)}_{m,i,R}$. For the first cell of a sweep in μ_m, the inflow $\psi^{(j+1)}_{m,i-1,R}$ is taken from the left boundary condition. In each other cell i, the inflow $\psi^{(j+1)}_{m,i-1,R}$ is the right-edge ψ_m value from the just-solved previous cell.

Sweeps for $\mu_m < 0$ are performed in a manner similar to that of $\mu_m > 0$. However, this sweep starts at the right end of the problem. For the first cell of a sweep in the negative direction, the inflow $\psi^{(j+1)}_{m,i+1,L}$ is taken from the right boundary condition. In keeping with the upwinding convention, the inflow into each cell i thereafter, $\psi^{(j+1)}_{m,i+1,L}$, is the left-edge ψ_m value from the

just-solved previous cell.

If a reflective boundary condition exists on the right boundary, the $\mu_m > 0$ half-sweep is executed first. If a reflective boundary condition exists on the left boundary, the $\mu_m < 0$ half-sweep is executed first.

1.7 Angular Discretization Scheme

The S_N angular discretization scheme utilizes some quadrature scheme in the angular domain. The Gauss N-point quadrature formula is used in this thesis, where N is an even, positive integer. Exact for all polynomials of degree $2N - 1$ or less, it is the most accurate quadrature scheme available. The points μ_m are chosen for integration over the range $\mu \in [-1, 1]$, where $\mu_m < 0$ for $m \leq N/2$ and $\mu_m > 0$ for $m > N/2$. Integration is performed over direction:

$$\phi_{\text{EAS}} = \int_{-1}^{1} \psi_{\text{EAS}}\, d\mu \approx \sum_{m=1}^{N} \psi(\mu_m) w_m, \tag{1.30}$$

where w_m represents the weight at quadrature point μ_m.

The symbol ψ_{EAS} represents the solution of the analytic problem Eqn. 1.3, known here as the *exact analytic solution* (EAS). If ψ includes subscripts or superscripts, it represents a parameter of the discretized solution for a given μ except when given explicitly as a function of x as in $\psi_{L,\text{in}}(x)$. The same convention applies to ϕ.

To form the S_N equation, Eqn. 1.3 is discretized in angle:

$$\mu \frac{\partial \psi}{\partial x}(\mu_m, x) + \sigma_t(x)\psi(\mu_m, x) = \frac{\sigma_s(x)}{2}\phi(x) + \frac{q(x)}{2}, \tag{1.31}$$

where μ_m is the m-th Gauss quadrature point. We reexpress Eqn. 1.31 in a more concise form:

$$\mu_m \frac{d\psi_m}{dx} + \sigma_t \psi_m = \frac{\sigma_s}{2}\phi + \frac{q}{2}, \tag{1.32}$$

where $\psi_m = \psi(\mu_m, x)$.

Applying the source iteration indices to the S_N equations, we get

$$\mu_m \frac{d\psi_m^{(\jmath+1)}}{dx} + \sigma_t \psi_m^{(\jmath+1)} = \frac{\sigma_s}{2}\phi^{(\jmath)} + \frac{q}{2}. \tag{1.33}$$

As previously noted, the S_N equations are solved using source iteration. The convergence of source iteration can also be accelerated. Acceleration is discussed in the next two sections.

1.8 Acceleration of Source Iterations

Source iteration alone is not viable for real-world problems in which $c \to 1$. For such slow-converging problems, *acceleration* becomes necessary. A variety of acceleration techniques have been developed to address this need.

Research into rapidly convergent methods for S_N problems has taken two overall paths. The first is the *linear acceleration* path. The other is the *nonlinear acceleration* path.

The S_2 acceleration scheme explored in this thesis lies on the nonlinear acceleration path. One scheme in widespread use is linear *Diffusion Synthetic Acceleration* (DSA), or linear *Diffusion Preconditioning*. Recalling Eqn. 1.18 and modifying the indices to indicate an accelerated scheme, the 1-D transport equation for DSA is

$$\mu \frac{\partial \psi^{(\ell+\frac{1}{2})}}{\partial x}(\mu, x) + \sigma_t \psi^{(\ell+\frac{1}{2})}(\mu, x) = \frac{\sigma_s}{2}\phi^{(\ell)}(x) + \frac{q(x)}{2}. \tag{1.34}$$

The other DSA equations are

$$\phi^{(\ell+\frac{1}{2})}(x) = \int_{-1}^{1} \psi^{(\ell+\frac{1}{2})}(\mu, x) du, \tag{1.35}$$

$$-\frac{1}{3\sigma_t}\frac{d^2F^{(\ell+1)}}{dx^2}(x) + \sigma_a F^{(\ell+1)}(x) = \sigma_s\left(\phi^{(\ell+\frac{1}{2})}(x) - \phi^{(\ell)}(x)\right), \tag{1.36}$$

$$\phi^{(\ell+1)}(x) = \phi^{(\ell+\frac{1}{2})}(x) + F^{(\ell+1)}(x). \tag{1.37}$$

These four equations are applied in sequence to compute $\psi^{(\ell+\frac{1}{2})}(\mu, x)$, $\phi^{(\ell+\frac{1}{2})}(x)$, $F^{(\ell+1)}(x)$, and $\phi^{(\ell+1)}(x)$, respectively. The function $F^{(\ell+1)}(x)$ is an estimate of the error of $\phi^{(\ell+1)}(x)$ with respect

to the exact solution $\phi(x)$. Equation 1.36 is the diffusion approximation in terms of F. The value in this approach is that it strongly attenuates modes of small Fourier eigenvalues, i.e. the modes which vary slowly in x. The lower error modes happen to be the modes for which SI exhibits poor convergence in for $c \to 1$. Furthermore, the spectral radius for DSA is approximately $0.2247c$. SI attenuates the higher modes quite effectively. Therefore, the combination of SI and diffusion approximation of the error utilized in DSA effectively attenuates error modes over the full Fourier spectrum, resulting in much accelerated convergence in otherwise slowly-converging SI problems.[3]

1.9 Nonlinear S_2 Acceleration

To derive the nonlinear S_2 transport equations, Eqn. 1.3 is integrated over $\mu \in [0, 1]$ and $\mu \in [-1, 0]$. For positive μ, the S_2 transport equation is

$$\int_0^1 \left[\mu \frac{\partial \psi}{\partial x} + \sigma_t \psi\right] \, d\mu = \int_0^1 \left[\frac{\sigma_s}{2}\phi + \frac{q}{2}\right] \, d\mu. \tag{1.38}$$

Next, split up and factor the integrals:

$$\frac{d}{dx}\int_0^1 \mu\psi \, d\mu + \sigma_t \int_0^1 \psi \, d\mu = \left[\frac{\sigma_s}{2}\phi + \frac{q}{2}\right] \int_0^1 d\mu. \tag{1.39}$$

Equation 1.3 must hold at each quadrature point μ_m. By solving for each corresponding $\psi_m = \psi(\mu_m, x)$, the resulting angular discretization of ψ can be used to compute the S_2, or *half-range*, scalar fluxes ϕ^+ and ϕ^-, where

$$\phi^+ = \int_0^1 \psi d\mu \approx \sum_{m=N/2+1}^{N} \psi_m w_m \tag{1.40}$$

and

$$\phi^- = \int_{-1}^0 \psi d\mu \approx \sum_{m=1}^{N/2} \psi_m w_m. \tag{1.41}$$

As is apparent from Eqns. 1.40 and 1.41, $\phi^+ + \phi^- = \int_{-1}^1 \psi d\mu$. Comparing with Eqn. 1.8, the scalar

flux ϕ can be expressed as

$$\phi = \phi^{+} + \phi^{-}. \tag{1.42}$$

The $\langle \mu^{+}(x) \rangle$ parameter, essentially a ψ-weighted average of μ over $\mu \in [0, 1]$, is defined by

$$\langle \mu^{+}(x) \rangle = \frac{\int_0^1 \mu \psi(\mu, x)\, d\mu}{\int_0^1 \psi(\mu, x)\, d\mu}. \tag{1.43}$$

Substituting Eqns. 1.40 and 1.43 into Eqn. 1.39, we obtain the nonlinear S_2 transport equation for the positive direction:

$$\frac{d}{dx}\left[\langle \mu^{+} \rangle \phi^{+}\right] + \sigma_t \phi^{+} \quad = \quad \frac{\sigma_s}{2}\phi + \frac{q}{2}. \tag{1.44}$$

Inserting the iteration indices into Eqns. 1.3, 1.43, and 1.44, we obtain the iteration equations for the acceleration scheme in positive μ:

$$\mu \frac{\partial \psi^{(\ell+\frac{1}{2})}}{\partial x}(\mu, x) + \sigma_t \psi^{(\ell+\frac{1}{2})}(\mu, x) = \frac{\sigma_s}{2}\phi^{(\ell)}(x) + \frac{q(x)}{2}, \tag{1.45}$$

$$\langle \mu^{+}(x) \rangle^{(\ell+\frac{1}{2})} = \frac{\int_0^1 \mu \psi^{(\ell+\frac{1}{2})}(\mu, x)\, d\mu}{\int_0^1 \psi^{(\ell+\frac{1}{2})}(\mu, x)\, d\mu}, \tag{1.46}$$

$$\frac{d}{dx}\left[\langle \mu^{+} \rangle^{(\ell+1)} \phi^{+,(\ell+1)}\right] + \sigma_t \phi^{+,(\ell+1)} \quad = \quad \frac{\sigma_s}{2}\phi^{(\ell+\frac{1}{2})} + \frac{q}{2}. \tag{1.47}$$

Likewise, for negative μ we obtain the the acceleration scheme iteration equations:

$$\mu \frac{\partial \psi^{(\ell+\frac{1}{2})}}{\partial x}(\mu, x) + \sigma_t \psi^{(\ell+\frac{1}{2})}(\mu, x) = \frac{\sigma_s}{2}\phi^{(\ell)}(x) + \frac{q(x)}{2}, \tag{1.48}$$

$$\langle \mu^{-}(x) \rangle^{(\ell+\frac{1}{2})} = \frac{\int_{-1}^0 \mu \psi^{(\ell+\frac{1}{2})}(\mu, x)\, d\mu}{\int_{-1}^0 \psi^{(\ell+\frac{1}{2})}(\mu, x)\, d\mu}, \tag{1.49}$$

$$\frac{d}{dx}\left[\langle\mu^-\rangle^{(\ell+1)}\phi^{-,(\ell+1)}\right] + \sigma_t\phi^{-,(\ell+1)} \quad = \quad \frac{\sigma_s}{2}\phi^{(\ell)} + \frac{q}{2}. \tag{1.50}$$

Adding the values obtained for $\phi^{+,(\ell+1)}$ and $\phi^{-,(\ell+1)}$ in Eqns. 1.47 and 1.50, respectively, the new scalar flux solution $\phi^{(\ell+1)}$ is obtained.

$$\phi^{(\ell+1)} = \phi^{+,(\ell+1)} + \phi^{-,(\ell+1)} \tag{1.51}$$

Equations 1.47 and 1.50 are solved using the multigrid method described in Chapter 3. The *uncompensated* relative error is given by Eqn. 1.53.

The problem to be solved is in two independent variables, directional cosine μ and 1-D spatial position x. We undertake to accelerate iterations in x only. For the S_N part of the cycle, a source iteration is taken over each μ_m, where μ_m is the m-th quadrature point in a Gauss quadrature set (with even order). The S_N sweep serves to update $\langle\mu\rangle$ in x. It is the solution for ϕ that is accelerated in the multigrid S_2 portion of the cycle, which takes $\langle\mu\rangle$ in x from the S_N sweep as input. The $\phi^{\pm,(\ell+1)}$ S_2 iterate resulting from the multigrid stage is then used on the right-hand side of Eqn. 1.18 for the next S_N sweep.

1.10 Convergence Test

Save for special cases such as pure-absorber material, the solution does not converge to the ICS in the trial space in a finite number of source iterations. Therefore, there must be a test condition to determine whether the solution after the ℓ-th iterate is "close enough" to the ICS. Ideally, this would involve taking a suitable norm of the error function, such as $\|\phi - \phi^{(\ell)}\|_{L^\infty}$. However, ϕ_{EAS} is not generally known, which necessitates a numerical solution in the first place. Therefore, a typical test is to measure the error between the two most recent iterates and compare to a prescribed threshold value, as in

$$\|\phi^{(\ell)} - \phi^{(\ell-1)}\|_{L^\infty} < \epsilon,\ \epsilon > 0. \tag{1.52}$$

In this thesis, an uncompensated relative error metric

$$E^{(\ell)}_{\text{rel,ucomp}} = \sup_{x\in[0,x_{\max}]} \frac{|\phi^{(\ell)} - \phi^{(\ell-1)}|}{|\phi^{(\ell)}|} < \epsilon,\ \epsilon > 0, \tag{1.53}$$

is utilized to keep the convergence test independent of the magnitude scale of $\tilde{\phi}$.

This test condition is adequate for highly absorbent materials but must be modified in order to be useful in highly diffusive problems, in which $c \to 1^-$. This is intimately related to the slow convergence for $c \to 1^-$ problems described in Section 1.4.1. Adams and Larsen explain why using Eqn. 1.52 or Eqn. 1.53 without corrective modifications leads to *false convergence*.[3]

2. ACCELERATED S_N SOLUTION ALGORITHM

2.1 Outline

1. Form the S_N SI equations.
2. Make an initial guess for $\tilde{\phi}$.
3. Perform S_N SI on the finest grid for each μ_m.
4. Use the values for $\langle \mu^+ \rangle$ and $\langle \mu^- \rangle$ from the S_N SI to form the equations for S_2 SI on the finest grid.
5. Solve S_2 nonlinear equation by multigrid method (see Chapter 3).

2.2 Discretization of Nonlinear S_2 Equation

Whereas for S_N the task is to solve for each ψ_m, in S_2 we solve for the half-range scalar fluxes ϕ^+ and ϕ^-. First, the S_2 equations on the finest grid are constructed from the S_N equations. We must integrate Eqn. 1.31 over $\mu > 0$ and $\mu < 0$ and insert the integration indices. The was done previously to arrive at Eqn. 1.47 and Eqn. 1.50.

Similar to Eqn. 1.19, the discretization of ϕ^+ and ϕ^- in cell i of width h_i is given by

$$\tilde{\phi}^{\pm}_{m,i}(x) = \frac{x_{i,R} - x}{h_i} \phi^{\pm}_{m,i,L} + \frac{x - x_{i,L}}{h_i} \phi^{\pm}_{m,i,R}, \tag{2.1}$$

where $\phi^{\pm}_{m,i,L}$ and $\phi^{\pm}_{m,i,R}$ are the parameters which define the LD solution $\tilde{\phi}_m$ in cell i.

To obtain the S_2 moment equations, $\phi^+_{m,i}(x)$ is substituted into Eqn. 1.47, which is then multiplied by each of the two weight functions, W_L from Eqn. 1.24 and W_R from Eqn. 1.25, and integrated over the cell width. The resulting S_2 moment equations for ϕ^+ are, for weight function

W_L,

$$\frac{1}{2}\left(\langle\mu_{i,L}^{+}\rangle^{(\ell+\frac{1}{2})}\phi_{i,L}^{+,(\jmath+1)}+\langle\mu_{i,R}^{+}\rangle^{(\ell+\frac{1}{2})}\phi_{i,R}^{+,(\jmath+1)}\right)+\frac{\sigma_{t,i}h_i}{2}\left(\frac{2}{3}\phi_{i,L}^{+,(\jmath+1)}+\frac{1}{3}\phi_{i,R}^{+,(\jmath+1)}\right)$$
$$=\frac{\sigma_{s,i}h_i}{2}\left(\frac{1}{3}\phi_{i,L}^{(\jmath)}+\frac{1}{6}\phi_{i,R}^{(\jmath)}\right)+\frac{h_i}{2}\left(\frac{1}{3}q_{i,L}+\frac{1}{6}q_{i,R}\right)+\langle\mu_{i-1,R}^{+}\rangle^{(\ell+\frac{1}{2})}\phi_{i-1,R}^{+,(\jmath+1)}, \tag{2.2}$$

and for weight function W_R,

$$\frac{1}{2}\left(\langle\mu_{i,R}^{+}\rangle^{(\ell+\frac{1}{2})}\phi_{i,R}^{+,(\jmath+1)}-\langle\mu_{i,L}^{+}\rangle^{(\ell+\frac{1}{2})}\phi_{i,L}^{+,(\jmath+1)}\right)+\frac{\sigma_{t,i}h_i}{2}\left(\frac{1}{3}\phi_{i,L}^{+,(\jmath+1)}+\frac{2}{3}\phi_{i,R}^{+,(\jmath+1)}\right)$$
$$=\frac{\sigma_{s,i}h_i}{2}\left(\frac{1}{6}\phi_{i,L}^{(\jmath)}+\frac{1}{3}\phi_{i,R}^{(\jmath)}\right)+\frac{h_i}{2}\left(\frac{1}{6}q_{i,L}+\frac{1}{3}q_{i,R}\right). \tag{2.3}$$

The S_2 moment equations for ϕ^- are obtained in a similar fashion from Eqn. 1.50. Substituting $\tilde{\phi}_{m,i}^{-}(x)$ for ϕ^-, the resulting S_2 moment equations for ϕ^- are, for weight function W_L,

$$\frac{1}{2}\left(\langle\mu_{i,R}^{-}\rangle^{(\ell+\frac{1}{2})}\phi_{i,R}^{-,(\jmath+1)}-\langle\mu_{i,L}^{-}\rangle^{(\ell+\frac{1}{2})}\phi_{i,L}^{-,(\jmath+1)}\right)+\frac{\sigma_{t,i}h_i}{2}\left(\frac{2}{3}\phi_{i,L}^{-,(\jmath+1)}+\frac{1}{3}\phi_{i,R}^{-,(\jmath+1)}\right)$$
$$=\frac{\sigma_{s,i}h_i}{2}\left(\frac{1}{3}\phi_{i,L}^{(\jmath)}+\frac{1}{6}\phi_{i,R}^{(\jmath)}\right)+\frac{h_i}{2}\left(\frac{1}{3}q_{i,L}+\frac{1}{6}q_{i,R}\right), \tag{2.4}$$

and for weight function W_R,

$$-\frac{1}{2}\left(\langle\mu_{i,L}^{-}\rangle^{(\ell+\frac{1}{2})}\phi_{i,L}^{-,(\jmath+1)}+\langle\mu_{i,R}^{-}\rangle^{(\ell+\frac{1}{2})}\phi_{i,R}^{-,(\jmath+1)}\right)+\frac{\sigma_{t,i}h_i}{2}\left(\frac{1}{3}\phi_{i,L}^{-,(\jmath+1)}+\frac{2}{3}\phi_{i,R}^{-,(\jmath+1)}\right)$$
$$=\frac{\sigma_{s,i}h_i}{2}\left(\frac{1}{6}\phi_{i,L}^{(\jmath)}+\frac{1}{3}\phi_{i,R}^{(\jmath)}\right)+\frac{h_i}{2}\left(\frac{1}{6}q_{i,L}+\frac{1}{3}q_{i,R}\right)-\langle\mu_{i+1,L}^{-}\rangle^{(\ell+\frac{1}{2})}\phi_{i+1,L}^{-,(\jmath+1)}. \tag{2.5}$$

Equations 2.2-2.5 give the system of S_2 equations on the finest grid only. The process for obtaining the S_2 moment equations on coarser grids is described in Section 3.2.

Several remarks are in order. First, we consider ϕ^+. In the discretized moment equations for $\tilde{\phi}^+$ (Eqns. 2.2 and 2.3), the two unknowns, $\phi_{i,L}^{+,(\jmath+1)}$ and $\phi_{i,R}^{+,(\jmath+1)}$, occur on the left-hand-side. $\phi_{i,L}^{+,(\jmath)}$ and $\phi_{i,R}^{+,(\jmath)}$ are known from the preceding SI, or from the initial guess for $\jmath=0$. The inflow flux $\phi_{i-1,R}^{+,(\jmath+1)}$ is known either from the preceding solve on the upwind cell from iteration $\jmath+1$ or from

the left boundary condition (cell 1). All $\langle\mu\rangle$ values have been computed from the most recent S_N transport sweep. All other parameters are known from the problem definition. Similar remarks apply to ϕ^- in Eqns. 2.4 and 2.5, except that the inflow flux for cell i is $\phi_{i+1,L}^{-,(j+1)}$ and taken from the right boundary condition for the rightmost cell.

The first S_2 sweep following the most recent S_N sweep is on the finest grid, taking initial guess $\phi^{\pm,(0)}$ from that S_N sweep. This S_2 sweep marks the beginning of the acceleration portion of the S_N cycle.

3. MULTIGRID METHOD FOR S_2 EQUATIONS

3.1 Multigrid Algorithm Outline

Our multigrid algorithm consists of two phases: a descent phase moving from coarse to fine grids, and an ascent phase moving from fine to coarse grids.

Descent Phase Perform sweep on current grid, update scalar fluxes, and project solution onto next coarse grid.

Ascent Phase Interpolate solution on current grid onto next fine grid.

The multigrid algorithm begins on the finest grid with the descent phase and continues until the coarsest grid is reached. A direct matrix inversion of the coarsest-grid S_2 equations is performed. Then, the ascent phase is begun and continues until the finest grid is reached. This completes one multigrid iteration. The first sweep on the finest grid is performed with the latest S_N scalar flux iterate.

3.2 Descending Between Grids

This section describes the finer-to-coarser grid transition. Cell enumeration starts with cell 1 on the left end. The cells of the finer grid are divided into adjacent pairs, so that, for odd i, cells i and $i+1$ on the finer grid are combined into cell $(i+1)/2$ on the coarser grid. This coarsening reduces the number of unknowns by half. Specifically, eight LD parameters (four in each fine cell) must be reduced to four LD parameters in the coarse cell.

Because $\tilde{\phi}$ is a weighted sum of the angular LD representations $\tilde{\psi}$ for each μ_m, $\tilde{\phi}$ is also in the LD form. However, this holds only for the finest grid. Projection of the S_2 moment equations onto a lower grid does not preserve the LD scheme on the coarse grid.

In descending one grid level to perform a subsequent SI, or, for the coarsest grid, a matrix solve, several objectives must be met:

1. Combine the moment equations of the left fine cell with the moment equations of the right fine cell to form the four moment equations in the combined coarse cell.

2. Eliminate the interior LD parameters, which are the four LD parameters at the edge between the left and right fine cells.

3. Provide for a means to reconstitute the LD parameters in Step 2 from the coarse-grid LD parameters during grid ascent.

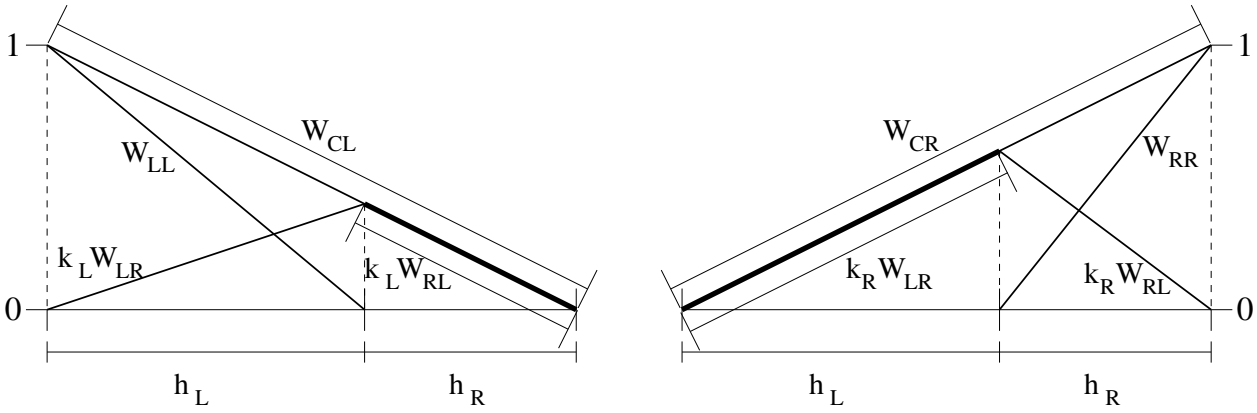

Figure 3.1: Coarse-cell weight functions can be represented in terms of the fine cell weight functions. Note that $k_L = h_R/h_C$ and $k_R = h_L/h_C$.

Weight Function $W(x)$	Description
W_{LL}	W_L in left fine cell
W_{LR}	W_R in left fine cell
W_{RL}	W_L in right fine cell
W_{RR}	W_R in right fine cell
W_{CL}	W_L in coarse cell
W_{CR}	W_R in coarse cell

Table 3.1: Weight functions for one coarse cell and its two constituent fine cells from the finer grid.

3.2.1 Forming Coarser Grid Moment Equations

The S_2 moment equations for coarse cell $(i+1)/2$ are derived from the moment equations for left fine cell i and right fine cell $i+1$. Each weight function defined in Table 3.1 equals zero outside of the cell for which it is defined. The maximum value of each weight function equals unity within the cell for which that weight function is defined. As shown in Fig. 3.1, the coarse cell width h_C is the sum of the left cell width h_L and the right cell width h_R. Since each of the six weight functions shown is linear in space, each of the coarse-cell weight functions W_{CL} and W_{CR} can be represented as a linear combination of three of the four fine-cell weight functions. By visual inspection, it is apparent that $W_{CL} = k_L W_{RL}$ in the right cell and $W_{CR} = k_R W_{LR}$ in the left cell. Also, the sum of two linear functions must be a linear function. Visual inspection reveals that W_{LL} and $k_L W_{LR}$ sum to W_{CL} at the edges of the left cell. Hence, $W_{CL} = W_{LL} + k_L W_{LR} + k_L W_{RL}$. Likewise, $W_{CR} = W_{RR} + k_R W_{RL} + k_R W_{LR}$.

Since W_{CL} is a linear function, its value at the common edge of the left and right cells must be $k_L = h_R/h_C$. Similarly, the value of W_{CR} at the common edge of the left and right cells must be $k_R = h_L/h_C$. The coarse-cell weight functions can thus be represented as the superposition of the fine weight functions.

$$W_{CL}(x) = W_{LL}(x) + \frac{h_R}{h_C}(W_{LR}(x) + W_{RL}(x)) \tag{3.1}$$

$$W_{RL}(x) = W_{RR}(x) + \frac{h_L}{h_C}(W_{LR}(x) + W_{RL}(x)) \tag{3.2}$$

Equations 3.1 and 3.2 are key to obtaining the S_2 moment equations for the coarse cell from the S_2 moment equations for the fine cells.

Given that each moment Eqns. 2.2-2.5 holds over the left and right cells, each also holds over the coarse cell. For the purpose of consolidation, we treat the pair of fine cells as one system of eight fine-cell moment equations in eight unknowns described by

$$\mathbf{L}_{8\times 8}\vec{\phi}_8 = \mathbf{S}_{8\times 8}\vec{\phi}_8 + \vec{q}_8. \tag{3.3}$$

Each row gives the coefficients of one fine-cell moment equation. The row ordering convention used here is defined in Table 3.2.

Row	Fine Cell	Moment Integrand	
		Weight Function	$\tilde{\phi}$ Operand
1	Left	W_{LL}	ϕ^+
2	Left	W_{LR}	ϕ^+
3	Left	W_{LL}	ϕ^-
4	Left	W_{LR}	ϕ^-
5	Right	W_{RL}	ϕ^+
6	Right	W_{RR}	ϕ^+
7	Right	W_{RL}	ϕ^-
8	Right	W_{RR}	ϕ^-

Table 3.2: Row order.

3.2.2 Row Reduction

Let us consider the $W(x) = W_{CL}$ moment equations for ϕ^+ and ϕ^-. Given the form $L\phi^\pm = S\phi^\pm + q$ and the fact that the moments on the cell are taken using

$$\int_h W(x) L\phi^\pm \, dx = \int_h W(x)(S\phi^\pm + q) \, dx \tag{3.4}$$

the coarse cell moment with $W_{CL}(x)$ can be expressed in terms of the fine cell moments by substituting the representation of $W_{CL}(x)$ given in Eqn. 3.1 for $W(x)$ in Eqn. 3.4:

$$\int_{h_C} \left[W_{LL} + \frac{h_R}{h_C}(W_{LR} + W_{RL}) \right] L\phi^\pm \, dx = \int_{h_C} \left[W_{LL} + \frac{h_R}{h_C}(W_{LR} + W_{RL}) \right] (S\phi^\pm + q) \, dx. \tag{3.5}$$

Separating the terms in Eqn. 3.5 so that each integral contains only one fine-cell $W(x)$,

$$\begin{aligned}
&\underbrace{\int_{h_C} W_{LL} L\phi^{\pm}\, dx}_{W_{LL}\text{ moment LHS}} + \frac{h_R}{h_C}\underbrace{\int_{h_C} W_{LR} L\phi^{\pm}\, dx}_{W_{LR}\text{ moment LHS}} + \frac{h_R}{h_C}\underbrace{\int_{h_C} W_{RL} L\phi^{\pm}\, dx}_{W_{RL}\text{ moment LHS}} \\
= \;& \underbrace{\int_{h_C} W_{LL}(S\phi^{\pm} + q)\, dx}_{W_{LL}\text{ moment RHS}} + \frac{h_R}{h_C}\underbrace{\int_{h_C} W_{LR}(S\phi^{\pm} + q)\, dx}_{W_{LR}\text{ moment RHS}} \\
+ \;& \frac{h_R}{h_C}\underbrace{\int_{h_C} W_{RL}(S\phi^{\pm} + q)\, dx}_{W_{RL}\text{ moment RHS}}. \qquad (3.6)
\end{aligned}$$

Because $W_{LL} = 0$ and $W_{LR} = 0$ outside of the left fine cell, their integration intervals can be shortened to the x spanned by h_L. Likewise, $W_{RL} = 0$ outside the right fine cell, so its integration interval can be shortened to the x spanned by h_R. Thus, Eqn. 3.5 can be expressed as a linear combination of these three fine-cell moment equations:

$$\int_{h_L} W_{LL} L\phi^{\pm}\, dx = \int_{h_L} W_{LL}(S\phi^{\pm} + q)\, dx \qquad (3.7)$$

$$\int_{h_L} W_{LR} L\phi^{\pm}\, dx = \int_{h_L} W_{LR}(S\phi^{\pm} + q)\, dx \qquad (3.8)$$

$$\int_{h_R} W_{RL} L\phi^{\pm}\, dx = \int_{h_R} W_{RL}(S\phi^{\pm} + q)\, dx \qquad (3.9)$$

For the following discussion, let $\mathbf{F}$ represent either matrix $\mathbf{L}_{8\times8}$ or $\mathbf{S}_{8\times8}$. For ϕ^{+}, Eqns. 3.7-3.9 correspond to rows 1, 2, and 5, respectively, in $\mathbf{F}$ (see Table 3.2). Let $\mathbf{C}_{4\times8}$ represent the 4×8 system of moment equations over the coarse cell, using the row order described for rows 1-4 in Table 3.2. For notational convenience, let $(\mathbf{M})_{Rn}$ be a vector representing row n of matrix $\mathbf{M}$. Rows 1 and 3 of $\mathbf{C}_{4\times8}$ are given by the linear combination described in Eqn. 3.6:

$$(\mathbf{C}_{4\times8})_{R1} = (\mathbf{F})_{R1} + \frac{h_R}{h_L + h_R}\left((\mathbf{F})_{R2} + (\mathbf{F})_{R5}\right) \qquad (3.10)$$

for W_{CL}-weighted $\tilde{\phi}^{+}$, and

$$(\mathbf{C}_{4\times 8})_{R3} = (\mathbf{F})_{R3} + \frac{h_R}{h_L + h_R}\left((\mathbf{F})_{R4} + (\mathbf{F})_{R7}\right) \tag{3.11}$$

for W_{CL}-weighted $\tilde{\phi}^{-}$.

By substituting W_{CR} for $W(x)$ as was done for W_{CL} in Eqn. 3.5 and repeating the ensuing derivation, it is found that

$$(\mathbf{C}_{4\times 8})_{R2} = (\mathbf{F})_{R6} + \frac{h_L}{h_L + h_R}\left((\mathbf{F})_{R2} + (\mathbf{F})_{R5}\right) \tag{3.12}$$

for W_{CR}-weighted $\tilde{\phi}^{+}$ and

$$(\mathbf{C}_{4\times 8})_{R4} = (\mathbf{F})_{R8} + \frac{h_L}{h_L + h_R}\left((\mathbf{F})_{R4} + (\mathbf{F})_{R7}\right) \tag{3.13}$$

for W_{CR}-weighted $\tilde{\phi}^{-}$.

This row-reduction scheme applies to $\mathbf{L}_{8\times 8}$, $\mathbf{S}_{8\times 8}$, and $\vec{q}_8$, to get $\mathbf{L}_{4\times 8}$, $\mathbf{S}_{4\times 8}$, and $\vec{q}_4$, respectively.

3.2.3 Column Reduction

The following convention is used here to characterize the LD parameters for $\tilde{\phi}$ in two fine cells to be combined in the coarse cell. For the fine cells, $\tilde{\phi}$ is characterized by the parameters ϕ^S_{CP}, where C (cell) is "L" to denote the left cell and "R" to denote the right cell, P (position) is "L" for the left $\tilde{\phi}$ parameter and "R" for the right $\tilde{\phi}$ LD parameter in the fine cell, and S is the sign for the direction: "$+$" for $\mu > 0$ and "$-$" for $\mu < 0$. For the coarse cell, LD parameters for $\tilde{\phi}$ are denoted by ϕ^S_P, using the definitions for P and S from above.

Row reduction leaves us with a 4×8 system, but we need a 4×4 system to solve in the coarse cell. Not only are there four equations and eight variables for the coarse cell, but the variables represent LD parameters of the fine cells, not the coarse cell. As indicated in Eqns. 3.14-3.17, LD parameters from the outer edges of the fine cells are used to initialize the corresponding LD

parameters in the coarse cell.

$$\phi_L^+ = \phi_{LL}^+ \tag{3.14}$$

$$\phi_R^+ = \phi_{RR}^+ \tag{3.15}$$

$$\phi_L^- = \phi_{LL}^- \tag{3.16}$$

$$\phi_R^- = \phi_{RR}^- \tag{3.17}$$

The LD $\tilde{\phi}$ parameters for the finer-grid cells are said to be *projected* onto the coarser-grid cells.

The columns representing the inner-edge fine-cell LD parameters can be eliminated by linearly combining them with columns representing the outer-edge fine-cell LD parameters. Here, this is achieved with the relations in Eqns. 3.18-3.21 for the γ parameters. The γ parameters are stored for interpolation of the inner-edge LD parameters from the outer-edge LD parameters passed from the coarser grid during the grid ascent stage.

$$\gamma_L^+ = \frac{2\phi_{LR}^+}{\phi_{LL}^+ + \phi_{RR}^+} \tag{3.18}$$

$$\gamma_R^+ = \frac{2\phi_{RL}^+}{\phi_{LL}^+ + \phi_{RR}^+} \tag{3.19}$$

$$\gamma_L^- = \frac{2\phi_{LR}^-}{\phi_{LL}^- + \phi_{RR}^-} \tag{3.20}$$

$$\gamma_R^- = \frac{2\phi_{RL}^-}{\phi_{LL}^- + \phi_{RR}^-} \tag{3.21}$$

Consider an LD function $\tilde{\psi}$ of x. Such a function is depicted in Fig. 3.2 for two fine-grid cells i and $i+1$ and one coarse-grid cell. In transitioning from the fine grid to the coarse grid, γ values are computed for each of $\psi_{i,R}$ and $\psi_{i+1,L}$. The γ values then represent multiplication factors relating each interior LD parameter to $\psi_{i+\frac{1}{2},A}$. Stated more explicitly, $\psi_{i,R} = \gamma_{i,R}\,\psi_{i+\frac{1}{2},A}$ and $\psi_{i+1,L} = \gamma_{i+1,L}\,\psi_{i+\frac{1}{2},A}$.

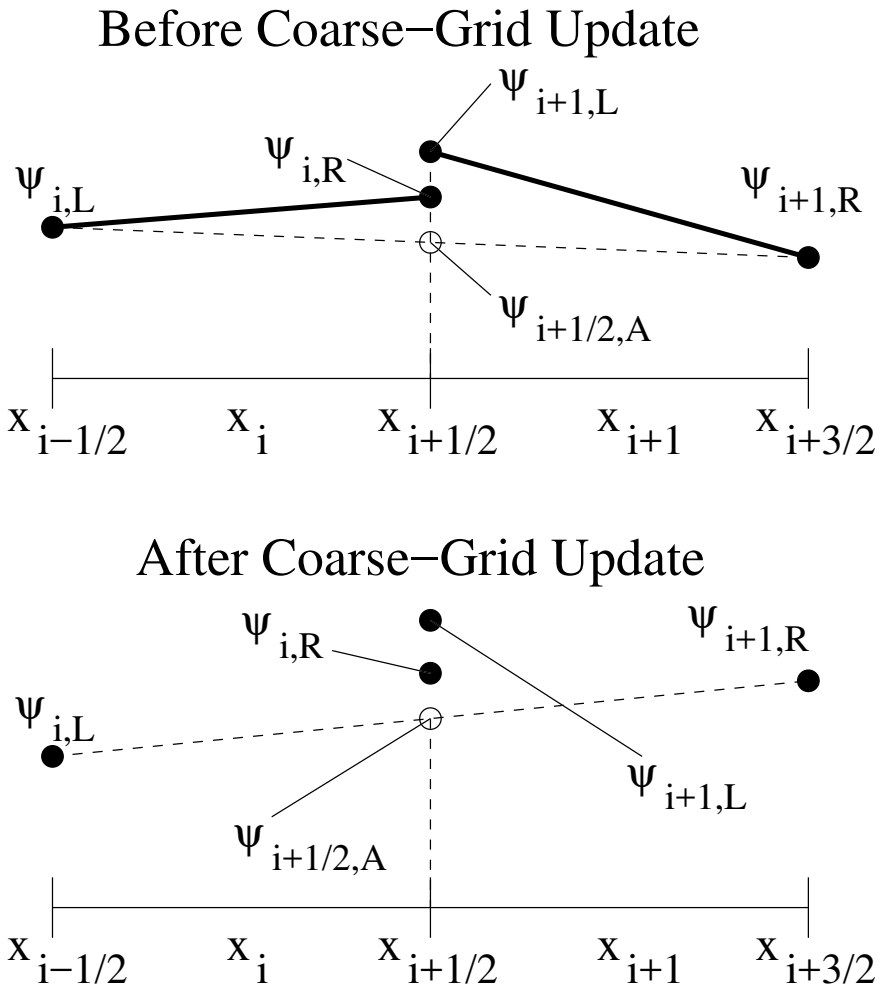

Figure 3.2: Graphical representation of the flux profile $\tilde{\psi}$ before and after the update of LD parameters $\psi_{i,L}$ and $\psi_{i+1,R}$ on the coarse grid. Here, $\psi_{i+\frac{1}{2},A}$ is the average value of the outer LD parameters. The γ factors for $\psi_{i+1,L}$ and $\psi_{i,R}$ remain unchanged before and after the coarse-grid update. In this particular depiction, $\tilde{\psi}$ is linear within each fine cell, which is true only on the finest grid. If the fine grid is not the finest, $\tilde{\psi}$ would be piecewise linear discontinuous within each fine cell.

Let $(\mathbf{M})_{Cm}$ be a vector representation of column m of matrix $\mathbf{M}$. Then, using the column order as defined in Table 3.3, $\mathbf{C}_{4\times 8}$ is transformed to $\mathbf{C}_{4\times 4}$ as follows.

$$(\mathbf{C}_{4\times 4})_{C1} = (\mathbf{C}_{4\times 8})_{C1} + \underbrace{\frac{\gamma_L^-}{2}(\mathbf{C}_{4\times 8})_{C2} + \frac{\gamma_R^-}{2}(\mathbf{C}_{4\times 8})_{C5}} \tag{3.22}$$

$$(\mathbf{C}_{4\times 4})_{C2} = (\mathbf{C}_{4\times 8})_{C6} + \overbrace{\frac{\gamma_L^-}{2}(\mathbf{C}_{4\times 8})_{C2} + \frac{\gamma_R^-}{2}(\mathbf{C}_{4\times 8})_{C5}} \tag{3.23}$$

$$(\mathbf{C}_{4\times 4})_{C3} = (\mathbf{C}_{4\times 8})_{C3} + \underbrace{\frac{\gamma_L^+}{2}(\mathbf{C}_{4\times 8})_{C4} + \frac{\gamma_R^+}{2}(\mathbf{C}_{4\times 8})_{C7}} \tag{3.24}$$

$$(\mathbf{C}_{4\times 4})_{C4} = (\mathbf{C}_{4\times 8})_{C8} + \overbrace{\frac{\gamma_L^+}{2}(\mathbf{C}_{4\times 8})_{C4} + \frac{\gamma_R^+}{2}(\mathbf{C}_{4\times 8})_{C7}} \tag{3.25}$$

The horizontal braces have been added to emphasize the commonality of terms in each pair of equations. This column-reduction scheme applies to each matrix $\mathbf{L}_{4\times 8}$ and $\mathbf{S}_{4\times 8}$ to get $\mathbf{L}_{4\times 4}$ and $\mathbf{S}_{4\times 4}$, respectively.

Column	Fine Cell	$\tilde{\phi}$ LD Variable
1	Left	$\phi_{i,L}^-$
2	Left	$\phi_{i,R}^-$
3	Left	$\phi_{i,L}^+$
4	Left	$\phi_{i,R}^+$
5	Right	$\phi_{i+1,L}^-$
6	Right	$\phi_{i+1,R}^-$
7	Right	$\phi_{i+1,L}^+$
8	Right	$\phi_{i+1,R}^+$

Table 3.3: Column order.

3.2.4 Updating the Solution on the Coarser Grid

Having obtained a 4×4 system for the coarser grid cell, the next step is to update the $\tilde{\phi}^{\pm}$ LD parameters on the coarser grid. If the coarsest grid specified for the problem is the current grid,

a global matrix solve is performed to update $\tilde{\phi}$, and the grid ascent begins. Otherwise, one S_2 sweep is performed on the grid according to Eqns. 2.2-2.5, and another descent step is performed as described in Section 3.2.

3.3 Ascending Between Grids

This section describes the coarser-grid-to-finer-grid transition. During the ascent stage of the V-cycle, we make one or more transitions from a finer grid to a coarser grid. We must be able to produce 8 LD parameters for two fine cells from one coarse cell. The updated parameters ϕ^+_{LL}, ϕ^+_{RR}, ϕ^-_{LL}, and ϕ^-_{RR}, on the fine grid are mapped from the coarse-grid parameters according to Eqns. 3.14-3.17. The parameters ϕ^+_{LR}, ϕ^+_{RL}, ϕ^-_{LR}, and ϕ^-_{RL} are interpolated using the relations given in Eqns. 3.18-3.21 with γ parameters stored during the most recent grid descent relating the current finer and coarser grids. This process of grid ascent continues until the finest grid is populated with the updated $\phi^{\pm}$ LD parameters.

Returning to Fig. 3.2, the ascent between grids can be visualized in terms of the updated coarse-grid LD parameters and the γ values stored during the descent. In Fig. 3.2, the outer LD parameters, and therefore $\psi_{i+\frac{1}{2},A}$, have been updated. By recalling the γ values and multiplying each by $\psi_{i+\frac{1}{2},A}$, the updated $\psi_{i,R}$ and $\psi_{i+1,L}$ are constructed from the updated value for $\psi_{i+\frac{1}{2},A}$ and the γ values. Thus, the updated $\psi_{i,R}$ and $\psi_{i+1,L}$ remain in the same ratio to $\psi_{i+\frac{1}{2},A}$ as during the descent.

Also of note, each of the γ values is obtained by dividing the corresponding $\tilde{\phi}$ LD parameter at the inside edge by the average of the $\tilde{\phi}$ LD parameters at the outside edges for the given direction. Consequently, if the fine cells are small enough that the exact solution is well-approximated within each cell by a linear function, the γ parameters should be close to unity.

3.4 Convergence Test in S_2

After the updated $\phi^{\pm}$ LD parameters have been obtained for the finest grid, $\phi^{+,(\ell)}$ and $\phi^{-,(\ell)}$ are added to obtain $\phi^{(\ell)}$. The new iterate $\phi^{(\ell)}$ is compared with the previous iterate as indicated in Eqn. 1.53. To avoid false convergence, it must be multiplied by a correction factor based on the spectral radius ρ. Since one cannot rely on the availability of an exact solution, ρ itself must be estimated from the $\tilde{\phi}$ iterates. The spectral radius ρ at iterate ℓ can be estimated by

$$\rho^{(\ell)} = \frac{\left\|\phi^{(\ell)} - \phi^{(\ell-1)}\right\|_{L^2}}{\left\|\phi^{(\ell-1)} - \phi^{(\ell-2)}\right\|_{L^2}}. \tag{3.26}$$

Three iterates of $\tilde{\phi}$ are required to compute $\rho^{(\ell)}$. Therefore, a minimum of three S_N cycles must be completed in order to determine convergence.

The *compensated* relative error is given as

$$E_{\text{rel}}^{(\ell)} = \frac{1}{1-\rho^{(\ell)}} \sup_{x\in[0,x_{\max}]} \frac{|\phi^{(\ell)} - \phi^{(\ell-1)}|}{|\phi^{(\ell)}|} < \epsilon,\ \epsilon > 0. \tag{3.27}$$

3.5 Negativities

Negativities in both the S_N ψ iterates and the S_2 ϕ iterates were observed during testing of this scheme. Lumping is one way to mitigate the occurrence of negativities. The fine-to-coarse projection scheme would need to be redefined to preserve lumping. This is an avenue to pursue in further work.

4. RESULTS

To test the multigrid algorithm and the associated Fourier analysis method, both were implemented in Python 3.5. In addition to core Python, the code used Python libraries NumPy, SciPy, and matplotlib. Results are presented for a multitude of problem input sets intended to uncover any weaknesses in the algorithm or flaws in the implementation.

Several checks are made in the implementation code to flag anomalous results.

- Test of negativity in the S_N $\tilde{\psi}$ iterate.
- Test of negativity in the S_2 $\tilde{\phi}^{\pm}$ iterate at multiple points in the multigrid algorithm.
- Test of negativity in each scalar flux iterate $\tilde{\phi}$ at the end of each S_N cycle.
- Fine grid S_2 matrix solve to compare against the multigrid-accelerated S_2 converged solution within each S_N cycle.
- Particle balance check in each region.

4.1 Constant-Solution S_2 with Fourier Convergence Analysis

One of the most important tasks in this thesis is characterization of the spectral radius of our multigrid method. A Fourier analysis method, detailed in Appendix C, was used to estimate the spectral radius for our multigrid method applied to the linear S_2 equations ($\mu = \pm\frac{1}{\sqrt{3}}$). This analysis assumes an infinite, periodic mesh, with a repeating structure consisting of two cells. The multigrid method analyzed was restricted to two grids: a fine grid and a coarse grid.

We performed accelerated S_N calculations to provide spectral radii for comparison with the theoretical spectral radii. Rather than accelerating higher-order S_N calculations, we accelerated S_2 calculations to ensure that the multigrid method would be applied to the linear S_2 acceleration equations. These calculations were performed in two cells with boundary conditions and an internal source that yielded a constant solution. The Fourier-computed spectral radii are compared to

the spectral radii estimated from the multigrid runs in Table 4.1. The iterations were terminated when the scalar fluxes were converged to a tolerance of 10^{-8}.

c	Cell Width (MFP)	V-Cycles Following First S_N Sweep	Spectral Radius	
			Estimated	Fourier
0.9	0.1	6	0.04	0.04
0.9	1	18	0.36	0.38
0.9	5	72	0.78	0.80
0.99	0.1	7	0.05	0.05
0.99	1	21	0.40	0.42
0.99	5	143	0.87	0.89
0.999	0.1	7	0.05	0.05
0.999	1	21	0.38	0.43
0.999	5	168	0.89	0.90
0.9999	0.1	7	0.05	0.05
0.9999	1	21	0.37	0.43
0.9999	5	173	0.89	0.91

Table 4.1: Run characteristics of homogeneous S_2 scenarios with theoretical Fourier spectral radius. Here, c is the ratio σ_s/σ_t. "Cell Width" is the width of each fine cell expressed in mean free paths. "V-Cycles Following First S_N Sweep" is the number of V-cycles needed to converge the S_2 solution to the problem defined by the average μ, or $\langle\mu\rangle$, parameters from the initial S_N sweep. "Spectral Radius: Estimated" refers to the spectral radius computed in the last three V-cycles in the series of V-cycles following the initial S_N sweep. "Spectral Radius: Fourier" refers to the spectral radius computed from Fourier analysis.

These data points show good agreement between the experimentally-computed and Fourier-computed spectral radii in each test scenario. The Fourier spectral radius is consistently higher than the experimental spectral radius. This is to be expected, as the Fourier technique models the problem as having infinite dimensions. Another factor contributing to the difference between the measured and theoretical spectral radii is the possible iterative convergence of the fine grid solution before iterative convergence of the spectral radius.

4.2 Homogeneous S_8

To test the algorithm for S_N problems with $N > 2$, several problems were run with homogeneous material composition, vacuum boundary conditions, and a constant internal source $q = 1 \frac{\text{neutron}}{\text{cm}^3 \text{ s}}$. Within these parameters, three different categories of test scenarios, as described in Table 4.2, were tested, each with varying c values and number of grids. All runs for the scenarios were performed to a tolerance of 10^{-5}.

Cell Width (MFP)	Cell Count	Problem Thickness (MFP)	Grid Count to Reach Single Coarse Grid
0.1	128	12.8	8
1	16	16	5
5	16	80	5

Table 4.2: Homogeneous S_8 test scenario categories. Test scenarios were run with these three cell-width values. Here, the fine-grid cell count "Cell Count" and "Problem Thickness" in mean free paths is given. "Grid Count to Reach Single Coarse Grid" refers to the total number of grid levels in a V-cycle needed to get a single-cell coarsest grid.

Test scenarios for each category in Table 4.2 were run with a multitude of c values and number of grid levels. In particular, pairs of scenarios differing only in number of grid levels were run. A "Grids" value of 2 represents the minimum number of grids required for multigrid acceleration. A "Grids" value greater than 2 is the constraint on the maximum number of grids imposed by the fine cell count, leaving a single cell on the coarsest grid. Results for these test scenarios are given in Table 4.3. As expected, higher c values require more V-cycles to converge. Also, scenarios run with higher grid counts have higher spectral radii than equivalent scenarios in two grids. Notably, the spectral radii exhibit the same trend as seen in Table 4.1 in that using thin fine-grid cells gives good acceleration, whereas using thick fine-grid cells gives poor acceleration.

Cell Width (MFP)	c	Grids	Total S_N Sweeps	Total V-Cycles	V-Cycles Following First S_N Sweep	Estimated S_2 Spectral Radius
0.1	0.9	2	5	17	5	0.05
0.1	0.9	8	5	25	9	0.25
0.1	0.99	2	6	20	5	0.06
0.1	0.99	8	6	51	17	0.47
0.1	0.999	2	6	20	5	0.06
0.1	0.999	8	6	57	18	0.50
0.1	0.9999	2	7	23	5	0.06
0.1	0.9999	8	9	58	19	0.51
1	0.9	2	5	26	10	0.40
1	0.9	5	5	38	17	0.53
1	0.99	2	7	48	14	0.46
1	0.99	5	7	104	39	0.75
1	0.999	2	8	59	14	0.47
1	0.999	5	7	122	45	0.77
1	0.9999	2	8	59	14	0.47
1	0.9999	5	8	134	46	0.78
5	0.9	2	5	93	42	0.80
5	0.9	5	5	95	41	0.80
5	0.99	2	7	290	83	0.89
5	0.99	5	6	572	177	0.95
5	0.999	2	10	577	92	0.92
5	0.999	5	9	2496	694	0.99
5	0.9999	2	13	1181	106	0.92
5	0.9999	5	11	4351	941	0.99

Table 4.3: Run characteristics of homogeneous S_8 scenarios. "Grids" refers to the the number of grid levels for each run. "Total S_N Sweeps" refers to the number of accelerated S_N iterations. "Total V-Cycles" denotes the total number of V-cycles performed on each run. "Estimated S_2 Spectral Radius" refers to the spectral radius computed in the last three V-cycles in the series of V-cycles following the initial S_N sweep. The other columns are as defined in Table 4.1.

The scenarios with more than two grids were also run with S_2 sweeps disabled on all grids but the finest, retaining the other components of the multigrid algorithm. The purpose of these runs was to explore the effect of descent-stage coarse-grid sweeps on acceleration. See Table 4.4. In comparing Table 4.3 and Table 4.4, equivalent runs require approximately three to five times as many V-cycles without coarse-grid sweeps to achieve the same convergence as with the sweeps. These results affirm that coarse-grid sweeps are indeed worth the cost.

Cell Width (MFP)	c	Grids	Total S_N Sweeps	Total V-Cycles	V-Cycles Following First S_N Sweep	Estimated S_2 Spectral Radius
0.1	0.9	8	5	103	50	0.81
0.1	0.99	8	6	260	99	0.89
0.1	0.999	8	6	311	110	0.90
0.1	0.9999	8	6	317	112	0.90
1	0.9	5	5	101	58	0.84
1	0.99	5	7	321	139	0.92
1	0.999	5	7	388	162	0.93
1	0.9999	5	8	398	165	0.93
5	0.9	5	5	168	75	0.89
5	0.99	5	7	2013	713	0.99
5	0.999	5	10	9019	2562	1.00
5	0.9999	5	12	16215	3466	1.00

Table 4.4: Run characteristics of homogeneous S_8 scenarios with multigrid-accelerated S_2 solution, sweeping on the finest grid only. The columns are as defined in Table 4.3.

In order to determine how well the scheme accelerates the S_N solution, the scenarios were rerun using S_N SI only. See Table 4.5. The acceleration does indeed work, as the number of S_N sweeps required to achieve convergence drops by about two orders of magnitude with acceleration.

Cell Width (MFP)	c	Total S_N Sweeps	
		SI Only	SI Plus S_2 Acceleration
0.1	0.9	97	5
0.1	0.99	445	6
0.1	0.999	681	6
1	0.9	102	5
1	0.99	558	7
1	0.999	986	8
5	0.9	111	5
5	0.99	1111	7
5	0.999	7742	10

Table 4.5: Run characteristics of homogeneous S_8 scenarios with finest-grid S_N sweeps only. "Total S_N Sweeps: SI Only" gives the number of S_N sweeps required to converge the S_N solution without acceleration. "Total S_N Sweeps: SI Plus S_2 Acceleration" gives the number of S_N sweeps required to converge the S_N solution with S_2 acceleration, reproduced here from Table 4.3 for comparison.

4.3 Modified Reed Problem

A problem proposed by Reed[4] was adapted to test the scheme in a problem with high material contrast. This modified Reed problem contains pure-absorber, vacuum, and pure-scattering regions. The input parameters for this 1-D, S_8 problem are described in Table 4.6. The left boundary is reflective, and the right boundary is a vacuum. The problem described here differs from the Reed problem in that $c = 0.9$ has been changed to $c = 1$ in regions 4 and 5. All runs for the modified Reed problem scenarios were performed to a tolerance of 10^{-7}.

	Regions				
	1	2	3	4	5
Width (cm)	2	1	2	1	2
σ_t (cm^{-1})	50	5	0	1	1
c	0	0	0	1	1
q (neutrons cm^{-3} s^{-1})	50	0	0	1	0

Table 4.6: Modified Reed problem: material properties by region.

Data from runs to solve the modified Reed problem are shown in Table 4.7 for a multitude of grid level counts. The comments in Section 4.2 on Table 4.3 about the "Grids" column apply here as well. Interestingly, unlike in the homogeneous S_8 problem, in the modified Reed problem there is little to no change in the accelerated S_2 spectral radius using two grids versus a higher grid count. As in the homogeneous S_8 problem, there is a penalty in number of V-cycles for using the maximum number of grids rather than two grids. This penalty is more modest overall for the modified Reed problem.

As was done in Section 4.2, the scenarios in Table 4.7 with more than two grids were rerun with S_2 sweeps disabled on all grids except the finest for the purpose of exploring the effect of descent-stage coarse-grid sweeps on acceleration. See Table 4.8. Here again, the coarse-grid sweeps play an important role in the acceleration scheme.

To determine the effectiveness of the non-linear S_2 acceleration of S_N iterations, it is necessary

Cell Count	Grids	Total S_N Sweeps	Total V-Cycles	V-Cycles Following First S_N Sweep	Estimated S_2 Spectral Radius
16	2	12	98	27	0.55
16	5	12	103	26	0.55
128	2	9	50	20	0.51
128	8	9	59	19	0.51
1024	2	9	37	13	0.50
1024	11	9	44	13	0.50

Table 4.7: Run characteristics of modified Reed problem with acceleration.

Cell Count	Grids	Total S_N Sweeps	Total V-Cycles	V-Cycles Following First S_N Sweep	Estimated S_2 Spectral Radius
16	5	11	166	51	0.73
128	8	9	148	51	0.73
1024	11	9	147	49	0.68

Table 4.8: Run characteristics of modified Reed problem with multigrid-accelerated S_2 solution, sweeping on the finest grid only.

to compare the metrics of accelerated solves to unaccelerated solves. This comparison is made in Table 4.9. As in the homogeneous S_8 problem, the acceleration scheme can work quite well in reducing the number S_N sweeps needed to converge the S_N solution.

Figure 4.1 is a plot of the solution for scalar flux with thin cells.

Cell Count	Total S_N Sweeps	
	SI Only	SI Plus S_2 Acceleration
16	111	12
128	111	9
1024	111	9

Table 4.9: Run characteristics of modified Reed problem with finest-grid S_N sweeps only. "Total S_N Sweeps: SI Only" gives the number of S_N sweeps required to converge the S_N solution without acceleration. "Total S_N Sweeps: SI Plus S_2 Acceleration" gives the number of S_N sweeps required to converge the S_N solution with S_2 acceleration, reproduced here from Table 4.7 for comparison.

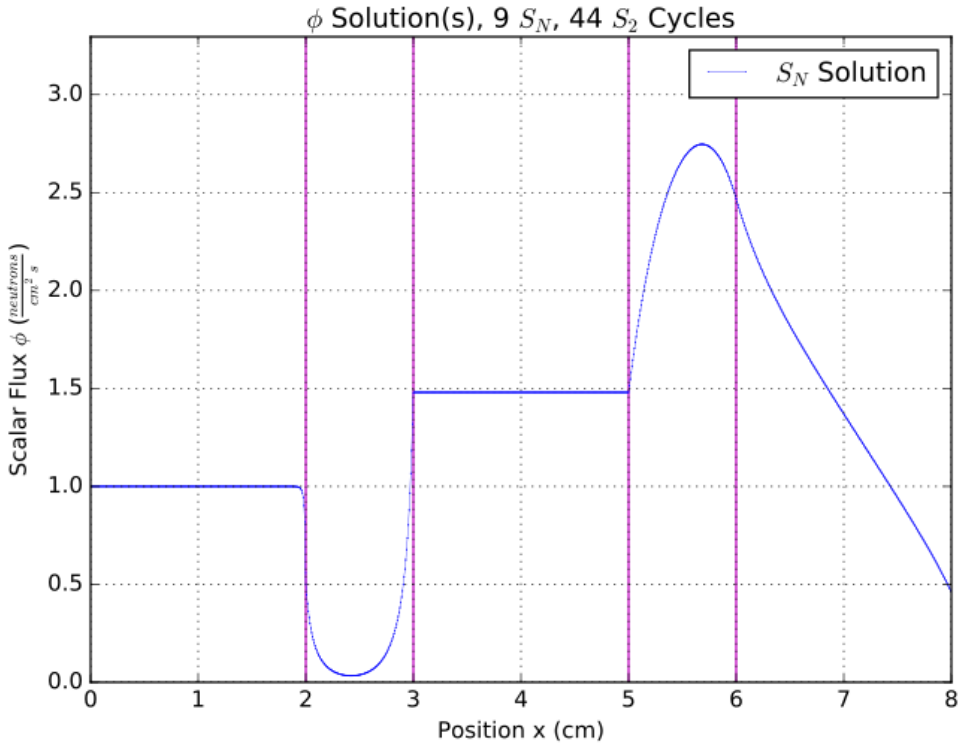

Figure 4.1: Computed scalar flux of modified Reed problem with 1024 fine cells and 11 grids. As enumerated in Table 4.6, the regions are numbered from left (Region 1) to right (Region 5).

5. CONCLUSION

The nonlinear S_2 acceleration scheme works best with optically-thin cells on the finest mesh and reasonably well with finest-mesh cells one mean free path thick. However, the scheme exhibits diminished acceleration for optically-thick cells on the finest mesh. The runs for the modified Reed problem suggest that the scheme is also effective for problems with high spatial contrast in material properties.

Comparing Tables 4.5 and 4.3, it is evident that multigrid S_2 provides considerable acceleration of the S_N problem for fine-grid cells up to about one mean-free-path thick. Having observed multiple cases in which the multigrid algorithm appreciably accelerates the S_2 solution, several cases tested with multigrid were tested again using multigrid with the modification that no S_2 source iterations were performed on coarse grids during descent. The purpose was to evaluate the importance of coarse-grid source iterations to the effectiveness of the multigrid algorithm. Comparing the homogeneous S_8 run results in Tables 4.4 and 4.3 and the modified Reed run results in Tables 4.8 and 4.7, it is seen that coarse-grid sweeps do indeed improve convergence of the solution. If descending to a single-cell coarsest grid, the total number of cells in the coarse grids is one less than the number of cells in the finest grid. So, within each V-cycle, sweeping on all the coarse grids should be about the same amount of work as sweeping the finest grid. In comparing the tables mentioned above, it is found that, except for one case, more than twice the number of V-cycles is required for each scenario if solved without the coarse-grid sweeps. These results indicate that coarse-grid sweeps do improve convergence, particularly for problems with optically-thin cells on the finest mesh.

The Fourier analysis undertaken for S_2 constant-solution cases yielded spectral radii which agree nicely with the test case runs. For each case, the Fourier spectral radius was somewhat greater than the values exhibited by the S_2 acceleration scheme. The difference was modest, with the case with the greatest disparity showing the empirical spectral radius to be 13% less than the Fourier spectral radius.

5.1 Future Work

The first item of interest in future work is to investigate the efficacy of lumped LD in eliminating negativities while not affecting convergence too adversely. Furthermore, lumped LD requires redefinition of the projection scheme. Presently, the results are not adequate to justify further work in 2-D. The degradation with cell thickness is a serious deficiency for many but not all applications.

REFERENCES

[1] J. J. Duderstadt, L. J. Hamilton, Nuclear Reactor Analysis, Wiley, 1976.

[2] E. E. Lewis, W. F. Miller Jr., Computational methods of neutron transport, John Wiley & Sons, New York, 1984.

[3] M. L. Adams, E. W. Larsen, Fast iterative methods for discrete-ordinates particle transport calculations, Progress in Nuclear Energy 40 (1) (2002) 3–159.

[4] W. H. Reed, New difference schemes for the neutron transport equation, Nuclear Science and Engineering 46 (2) (1971) 309–314.

APPENDIX A

S_N MOMENT EQUATIONS

The angle-discretized transport equation Eqn. 1.33 is the starting point for the ensuing S_N LD moment equation derivations.

A.1 Moment Equation for $\mu > 0$ and $B = B_L$

First, multiply Eqn. 1.33 by B_L (defined in Eqn. 1.24), substitute $\tilde{\psi}_{m,i}(x)$ from Eqn. 1.19, and integrate over cell width h_i.

$$\begin{aligned} & \int_{h_i} \mu_m B_L(x) \frac{d\tilde{\psi}_{m,i}}{dx}(x)\, dx + \int_{h_i} \sigma_{t,i} B_L(x) \tilde{\psi}_{m,i}(x)\, dx \\ = & \int_{h_i} B_L(x) \frac{\sigma_{s,i}}{2} \tilde{\phi}_i(x)\, dx + \int_{h_i} B_L(x) \frac{q_i(x)}{2}\, dx \end{aligned} \tag{A.1}$$

$$\begin{aligned} & \mu_m \int_{h_i} B_L(x) \frac{d\tilde{\psi}_{m,i}}{dx}(x)\, dx + \sigma_{t,i} \int_{h_i} B_L(x) \tilde{\psi}_{m,i}(x)\, dx \\ = & \frac{\sigma_{s,i}}{2} \int_{h_i} B_L(x) \tilde{\phi}_i(x)\, dx + \frac{1}{2} \int_{h_i} B_L(x) q_i(x)\, dx \end{aligned} \tag{A.2}$$

Apply integration by parts to the integral in the first LHS term.

$$\int_{h_i} B_L(x) \frac{d\tilde{\psi}_{m,i}}{dx}(x)\, dx = \left[B_L(x) \tilde{\psi}_{m,i}(x) \right]_{x_{i-\frac{1}{2}}}^{x_{i+\frac{1}{2}}} - \int_{x_{i-\frac{1}{2}}}^{x_{i+\frac{1}{2}}} \frac{dB_L}{dx}(x) \tilde{\psi}_{m,i}(x)\, dx \tag{A.3}$$

Substituting the expressions for B_L and $\tilde{\psi}_{m,i}$ into Eqn. A.3, the boundary term evaluates to

$$\left[\frac{x_{i+\frac{1}{2}} - x}{h_i} \left(\frac{x_{i+\frac{1}{2}} - x}{h_i} \psi_m(x_{i-\frac{1}{2}}) + \frac{x - x_{i-\frac{1}{2}}}{h_i} \psi_m(x_{i+\frac{1}{2}}) \right) \right]_{x_{i-\frac{1}{2}}}^{x_{i+\frac{1}{2}}} = -\psi_m(x_{i-\frac{1}{2}}). \tag{A.4}$$

Substituting the LD parameters dictated by the upwinding convention, the boundary term becomes

$$\left[\frac{x_{i+\frac{1}{2}}-x}{h_i}\left(\frac{x_{i+\frac{1}{2}}-x}{h_i}\psi_{m,i-1,R}+\frac{x-x_{i-\frac{1}{2}}}{h_i}\psi_{m,i,R}\right)\right]_{x_{i-\frac{1}{2}}}^{x_{i+\frac{1}{2}}}=-\psi_{m,i-1,R}. \tag{A.5}$$

The RHS integral of Eqn. A.3 becomes

$$\begin{aligned}
&-\int_{x_{i-\frac{1}{2}}}^{x_{i+\frac{1}{2}}}-\frac{1}{h_i}\left(\frac{x_{i+\frac{1}{2}}-x}{h_i}\psi_{m,i,L}+\frac{x-x_{i-\frac{1}{2}}}{h_i}\psi_{m,i,R}\right)\,dx\\
=&\ \frac{1}{h_i^2}\left[\psi_{m,i,L}\int_{x_{i-\frac{1}{2}}}^{x_{i+\frac{1}{2}}}(x_{i+\frac{1}{2}}-x)\,dx+\psi_{m,i,R}\int_{x_{i-\frac{1}{2}}}^{x_{i+\frac{1}{2}}}(x-x_{i-\frac{1}{2}})\,dx\right]\\
=&\ \frac{1}{h_i^2}\left(-\frac{\psi_{m,i,L}}{2}\left[(x_{i+\frac{1}{2}}-x)^2\right]_{x_{i-\frac{1}{2}}}^{x_{i+\frac{1}{2}}}+\frac{\psi_{m,i,R}}{2}\left[(x-x_{i-\frac{1}{2}})^2\right]_{x_{i-\frac{1}{2}}}^{x_{i+\frac{1}{2}}}\right)\\
=&\ \frac{\psi_{m,i,L}}{2}+\frac{\psi_{m,i,R}}{2}.
\end{aligned} \tag{A.6}$$

Substituting the foregoing results into the first LHS term of Eqn. A.2, it becomes

$$-\mu_m\psi_{m,i-1,R}+\frac{\mu_m}{2}(\psi_{m,i,L}+\psi_{m,i,R}). \tag{A.7}$$

Next, we evaluate the second LHS term of Eqn. A.2, by substituting the expressions for $B_L(x)$ and $\tilde{\psi}_{m,i}(x)$.

$$\begin{aligned}
&\sigma_{t,i}\int_{h_i}B_L(x)\tilde{\psi}_{m,i}(x)\,dx\\
=&\ \sigma_{t,i}\int_{h_i}\frac{x_{i+\frac{1}{2}}-x}{h_i}\left(\frac{x_{i+\frac{1}{2}}-x}{h_i}\psi_{m,i,L}+\frac{x-x_{i-\frac{1}{2}}}{h_i}\psi_{m,i,R}\right)\,dx\\
=&\ \frac{\sigma_{t,i}}{h_i^2}\left(\psi_{m,i,L}\underbrace{\int_{h_i}(x_{i+\frac{1}{2}}-x)^2\,dx}_{\text{Integral }A}+\psi_{m,i,R}\underbrace{\int_{h_i}(x_{i+\frac{1}{2}}-x)(x-x_{i-\frac{1}{2}})\,dx}_{\text{Integral }B}\right)
\end{aligned} \tag{A.8}$$

The evaluation of Integral A is straightforward.

$$\int_{h_i} (x_{i+\frac{1}{2}} - x)^2 \, dx = -\frac{1}{3} \left[(x_{i+\frac{1}{2}} - x)^3 \right]_{x_{i-\frac{1}{2}}}^{x_{i+\frac{1}{2}}} = \frac{h_i^3}{3} \tag{A.9}$$

An integration-by-parts approach is taken for Integral B.

$$\begin{aligned}
& \int_{h_i} \underbrace{(x_{i+\frac{1}{2}} - x)}\underbrace{(x - x_{i-\frac{1}{2}})} \, dx \\
= & \left[(x_{i+\frac{1}{2}} - x) \frac{(x - x_{i-\frac{1}{2}})^2}{2} \right]_{x_{i-\frac{1}{2}}}^{x_{i+\frac{1}{2}}} - \int_{h_i} -\frac{(x - x_{i-\frac{1}{2}})^2}{2} \, dx \\
= & \frac{1}{2} \left[(x_{i+\frac{1}{2}} - x)(x - x_{i-\frac{1}{2}})^2 \right]_{x_{i-\frac{1}{2}}}^{x_{i+\frac{1}{2}}} + \frac{1}{6} \left[(x - x_{i-\frac{1}{2}})^3 \right]_{x_{i-\frac{1}{2}}}^{x_{i+\frac{1}{2}}} \\
= & \frac{h_i^3}{6}
\end{aligned} \tag{A.10}$$

Substituting the results from Eqn. A.9 and Eqn. A.10 into Eqn. A.8, the second LHS term of Eqn. A.2 evaluates to

$$\frac{\sigma_{t,i} h_i}{2} \left(\frac{2}{3} \psi_{m,i,L} + \frac{1}{3} \psi_{m,i,R} \right). \tag{A.11}$$

To evaluate the first RHS term of Eqn. A.2, substitute the B_L and the LD representation of ϕ. Since the integral is identical in form to the integral in the second LHS term of Eqn. A.2, that result can be applied to this term also.

$$\begin{aligned}
& \frac{\sigma_{s,i}}{2} \int_{h_i} B_L(x) \tilde{\phi}(x) \, dx \\
= & \frac{\sigma_{s,i}}{2} \int_{h_i} \frac{x_{i+\frac{1}{2}} - x}{h_i} \left(\frac{x_{i+\frac{1}{2}} - x}{h_i} \phi_{i,L} + \frac{x - x_{i-\frac{1}{2}}}{h_i} \phi_{i,R} \right) dx \\
= & \frac{\sigma_{s,i} h_i}{2} \left(\frac{1}{3} \phi_{i,L} + \frac{1}{6} \phi_{i,R} \right)
\end{aligned} \tag{A.12}$$

The second RHS term of Eqn. A.2 is evaluated in a similar fashion.

$$\begin{aligned} & \frac{1}{2}\int_{h_i} B_L(x) q_i(x)\, dx \\ = \; & \frac{1}{2}\int_{h_i} \frac{x_{i+\frac{1}{2}} - x}{h_i}\left(\frac{x_{i+\frac{1}{2}} - x}{h_i} q_{i,L} + \frac{x - x_{i-\frac{1}{2}}}{h_i} q_{i,R}\right) dx \\ = \; & \frac{h_i}{2}\left(\frac{1}{3} q_{i,L} + \frac{1}{6} q_{i,R}\right) \end{aligned} \tag{A.13}$$

Substituting each of the terms in Eqn. A.1 with their evaluated expressions in Eqn. A.7, Eqn. A.11, Eqn. A.12, and Eqn. A.13, the resulting moment equation is

$$\begin{aligned} & -\mu_m \psi_{m,i-1,R} + \frac{\mu_m}{2}(\psi_{m,i,L} + \psi_{m,i,R}) + \frac{\sigma_{t,i} h_i}{2}\left(\frac{2}{3}\psi_{m,i,L} + \frac{1}{3}\psi_{m,i,R}\right) \\ = \; & \frac{\sigma_{s,i} h_i}{2}\left(\frac{1}{3}\phi_{i,L} + \frac{1}{6}\phi_{i,R}\right) + \frac{h_i}{2}\left(\frac{1}{3} q_{i,L} + \frac{1}{6} q_{i,R}\right). \end{aligned} \tag{A.14}$$

By inserting the iteration indices and moving the first term to the RHS, we arrive at the SI form in Eqn. 1.26 in which both unknowns are on the LHS.

A.2 Moment Equation for $\mu > 0$ and $B = B_R$

Multiply Eqn. 1.33 by B_R (defined in Eqn. 1.25), substitute $\tilde{\psi}_{m,i}(x)$ from Eqn. 1.19, and integrate over cell width h_i.

$$\begin{aligned} & \int_{h_i} \mu_m B_R(x) \frac{d\tilde{\psi}_{m,i}}{dx}(x)\, dx + \int_{h_i} \sigma_{t,i} B_R(x) \tilde{\psi}_{m,i}(x)\, dx \\ = \; & \int_{h_i} B_R(x) \frac{\sigma_{s,i}}{2} \tilde{\phi}_i(x)\, dx + \int_{h_i} B_R(x) \frac{q_i(x)}{2}\, dx \end{aligned} \tag{A.15}$$

$$\begin{aligned} & \mu_m \int_{h_i} B_R(x) \frac{d\tilde{\psi}_{m,i}}{dx}(x)\, dx + \sigma_{t,i} \int_{h_i} B_R(x) \tilde{\psi}_{m,i}(x)\, dx \\ = \; & \frac{\sigma_{s,i}}{2} \int_{h_i} B_R(x) \tilde{\phi}_i(x)\, dx + \frac{1}{2} \int_{h_i} B_R(x) q_i(x)\, dx \end{aligned} \tag{A.16}$$

Apply integration by parts to the integral in the first LHS term.

$$\int_{h_i} B_R(x)\frac{d\tilde{\psi}_{m,i}}{dx}(x)\,dx = \left[B_R(x)\tilde{\psi}_{m,i}(x)\right]_{x_{i-\frac{1}{2}}}^{x_{i+\frac{1}{2}}} - \int_{x_{i-\frac{1}{2}}}^{x_{i+\frac{1}{2}}} \frac{dB_R}{dx}(x)\tilde{\psi}_{m,i}(x)\,dx \tag{A.17}$$

Substituting the expressions for B_R and $\tilde{\psi}_{m,i}$ into Eqn. A.17, the boundary term evaluates to

$$\left[\frac{x-x_{i-\frac{1}{2}}}{h_i}\left(\frac{x_{i+\frac{1}{2}}-x}{h_i}\psi_m(x_{i-\frac{1}{2}}) + \frac{x-x_{i-\frac{1}{2}}}{h_i}\psi_m(x_{i+\frac{1}{2}})\right)\right]_{x_{i-\frac{1}{2}}}^{x_{i+\frac{1}{2}}} = \psi_m(x_{i+\frac{1}{2}}). \tag{A.18}$$

Substituting the LD parameters dictated by the upwinding convention, the boundary term becomes

$$\left[\frac{x-x_{i-\frac{1}{2}}}{h_i}\left(\frac{x_{i+\frac{1}{2}}-x}{h_i}\psi_{m,i-1,R} + \frac{x-x_{i-\frac{1}{2}}}{h_i}\psi_{m,i,R}\right)\right]_{x_{i-\frac{1}{2}}}^{x_{i+\frac{1}{2}}} = \psi_{m,i,R}. \tag{A.19}$$

The RHS integral of Eqn. A.17 becomes

$$\begin{aligned}
& -\int_{x_{i-\frac{1}{2}}}^{x_{i+\frac{1}{2}}} \frac{1}{h_i}\left(\frac{x_{i+\frac{1}{2}}-x}{h_i}\psi_{m,i,L} + \frac{x-x_{i-\frac{1}{2}}}{h_i}\psi_{m,i,R}\right)\,dx \\
= & -\frac{1}{h_i^2}\left[\psi_{m,i,L}\int_{x_{i-\frac{1}{2}}}^{x_{i+\frac{1}{2}}}(x_{i+\frac{1}{2}}-x)\,dx + \psi_{m,i,R}\int_{x_{i-\frac{1}{2}}}^{x_{i+\frac{1}{2}}}(x-x_{i-\frac{1}{2}})\,dx\right] \\
= & -\frac{1}{h_i^2}\left(-\frac{\psi_{m,i,L}}{2}\left[(x_{i+\frac{1}{2}}-x)^2\right]_{x_{i-\frac{1}{2}}}^{x_{i+\frac{1}{2}}} + \frac{\psi_{m,i,R}}{2}\left[(x-x_{i-\frac{1}{2}})^2\right]_{x_{i-\frac{1}{2}}}^{x_{i+\frac{1}{2}}}\right) \\
= & -\frac{\psi_{m,i,L}}{2} - \frac{\psi_{m,i,R}}{2}.
\end{aligned} \tag{A.20}$$

Substituting the foregoing results into the first LHS term of Eqn. A.16, it becomes

$$\mu_m\psi_{m,i,R} - \frac{\mu_m}{2}(\psi_{m,i,L}+\psi_{m,i,R}) = \frac{\mu_m}{2}(-\psi_{m,i,L}+\psi_{m,i,R}). \tag{A.21}$$

Next, we evaluate the second LHS term of Eqn. A.16 by substituting the expressions for $B_R(x)$

and $\tilde{\psi}_{m,i}(x)$.

$$\begin{aligned}
& \sigma_{t,i} \int_{h_i} B_R(x) \tilde{\psi}_{m,i}(x)\, dx \\
= \; & \sigma_{t,i} \int_{h_i} \frac{x - x_{i-\frac{1}{2}}}{h_i} \left(\frac{x_{i+\frac{1}{2}} - x}{h_i} \psi_{m,i,L} + \frac{x - x_{i-\frac{1}{2}}}{h_i} \psi_{m,i,R} \right) dx \\
= \; & \frac{\sigma_{t,i}}{h_i^2} \left(\psi_{m,i,L} \underbrace{\int_{h_i} (x - x_{i-\frac{1}{2}})(x_{i+\frac{1}{2}} - x)\, dx}_{\text{Integral } B} + \psi_{m,i,R} \underbrace{\int_{h_i} (x - x_{i-\frac{1}{2}})^2\, dx}_{\text{Integral } A} \right)
\end{aligned} \tag{A.22}$$

By observing its equivalence to Integral B in Eqn. A.22, Integral B in Eqn. A.22 is simply $h_i^3/6$, as given in Eqn. A.10. The evaluation of Integral A is straightforward.

$$\int_{h_i} (x - x_{i-\frac{1}{2}})^2\, dx = \frac{1}{3} \left[(x - x_{i-\frac{1}{2}})^3 \right]_{x_{i-\frac{1}{2}}}^{x_{i+\frac{1}{2}}} = \frac{h_i^3}{3} \tag{A.23}$$

Substituting the results from Eqn. A.23 and Eqn. A.10 into Eqn. A.22, the second LHS term of Eqn. A.16 evaluates to

$$\frac{\sigma_{t,i} h_i}{2} \left(\frac{1}{3} \psi_{m,i,L} + \frac{2}{3} \psi_{m,i,R} \right) \tag{A.24}$$

To evaluate the first RHS term of Eqn. A.16, substitute the B_R and the LD representation of ϕ. Since the integral is identical in form to the integral in the second LHS term of Eqn. A.16, that result can be applied to this term also.

$$\frac{\sigma_{s,i}}{2} \int_{h_i} B_R(x) \tilde{\phi}(x)\, dx = \frac{\sigma_{s,i} h_i}{2} \left(\frac{1}{6} \phi_{i,L} + \frac{1}{3} \phi_{i,R} \right) \tag{A.25}$$

The second RHS term of Eqn. A.16 is evaluated in a similar fashion.

$$\frac{1}{2} \int_{h_i} B_R(x) q_i(x)\, dx = \frac{h_i}{2} \left(\frac{1}{6} q_{i,L} + \frac{1}{3} q_{i,R} \right) \tag{A.26}$$

Substituting each of the terms in Eqn. A.15 with their evaluated expressions in Eqn. A.21,

Eqn. A.24, Eqn. A.25, and Eqn. A.26, the resulting moment equation is

$$\begin{aligned} & \frac{\mu_m}{2}(-\psi_{m,i,L}+\psi_{m,i,R})+\frac{\sigma_{t,i}h_i}{2}\left(\frac{1}{3}\psi_{m,i,L}+\frac{2}{3}\psi_{m,i,R}\right) \\ = \; & \frac{\sigma_{s,i}h_i}{2}\left(\frac{1}{6}\phi_{i,L}+\frac{1}{3}\phi_{i,R}\right)+\frac{h_i}{2}\left(\frac{1}{6}q_{i,L}+\frac{1}{3}q_{i,R}\right). \end{aligned} \tag{A.27}$$

By inserting the iteration indices, we arrive at the SI form in Eqn. 1.27 in which both unknowns are on the LHS.

A.3 Moment Equation for $\mu < 0$ and $B = B_L$

The derivation of this moment equation is very similar to the derivation of the case for $\mu < 0$ and $B = B_L$ in Section A.1. The only difference is in the treatment of the boundary term component of the first LHS term of Eqn. A.2, as the sign change in μ reverses the upwinding direction.

Consider the representation of the boundary term in Eqn. A.4. Replace with the LD parameters for upwinding.

$$\left[\frac{x_{i+\frac{1}{2}}-x}{h_i}\left(\frac{x_{i+\frac{1}{2}}-x}{h_i}\psi_{m,i,L}+\frac{x-x_{i-\frac{1}{2}}}{h_i}\psi_{m,i+1,L}\right)\right]_{x_{i-\frac{1}{2}}}^{x_{i+\frac{1}{2}}}=-\psi_{m,i,L} \tag{A.28}$$

Adding the component from Eqn. A.6, the first LHS term of Eqn. A.2 becomes

$$\frac{\mu_m}{2}(-\psi_{m,i,L}+\psi_{m,i,R}). \tag{A.29}$$

The resulting moment equation is

$$\begin{aligned} & \frac{\mu_m}{2}(-\psi_{m,i,L}+\psi_{m,i,R})+\frac{\sigma_{t,i}h_i}{2}\left(\frac{2}{3}\psi_{m,i,L}+\frac{1}{3}\psi_{m,i,R}\right) \\ = \; & \frac{\sigma_{s,i}h_i}{2}\left(\frac{1}{3}\phi_{i,L}+\frac{1}{6}\phi_{i,R}\right)+\frac{h_i}{2}\left(\frac{1}{3}q_{i,L}+\frac{1}{6}q_{i,R}\right). \end{aligned} \tag{A.30}$$

By inserting the iteration indices, we arrive at the SI form in Eqn. 1.28 in which both unknowns

are on the LHS.

A.4 Moment Equation for $\mu < 0$ and $B = B_R$

The derivation of this moment equation is very similar to the derivation of the case for $\mu < 0$ and $B = B_R$ in Section A.2. The only difference is in the treatment of the boundary term component of the first LHS term of Eqn. A.16, as the sign change in μ reverses the upwinding direction.

Consider the representation of the boundary term in Eqn. A.18. Replace with the LD parameters for upwinding.

$$\left[\frac{x - x_{i-\frac{1}{2}}}{h_i}\left(\frac{x_{i+\frac{1}{2}} - x}{h_i}\psi_{m,i,L} + \frac{x - x_{i-\frac{1}{2}}}{h_i}\psi_{m,i+1,L}\right)\right]_{x_{i-\frac{1}{2}}}^{x_{i+\frac{1}{2}}} = \psi_{m,i+1,L} \tag{A.31}$$

Adding the component from Eqn. A.20, the first LHS term of Eqn. A.16 becomes

$$\mu_m\psi_{m,i+1,L} - \frac{\mu_m}{2}(\psi_{m,i,L} + \psi_{m,i,R}). \tag{A.32}$$

The resulting moment equation is

$$\begin{aligned} & \mu_m\psi_{m,i+1,L} - \frac{\mu_m}{2}(\psi_{m,i,L} + \psi_{m,i,R}) + \frac{\sigma_{t,i}h_i}{2}\left(\frac{1}{3}\psi_{m,i,L} + \frac{2}{3}\psi_{m,i,R}\right) \\ = \; & \frac{\sigma_{s,i}h_i}{2}\left(\frac{1}{6}\phi_{i,L} + \frac{1}{3}\phi_{i,R}\right) + \frac{h_i}{2}\left(\frac{1}{6}q_{i,L} + \frac{1}{3}q_{i,R}\right) \end{aligned} \tag{A.33}$$

By inserting the iteration indices, we arrive at the SI form in Eqn. 1.29 in which both unknowns are on the LHS.

APPENDIX B

COMPUTATION OF NORMS IN LD

In taking the norm of the error between iterates, one consideration is to compute the norm by considering only the differences of the LD cell-edge fluxes rather than from an integral over the spatial domain. This makes no difference in computing the relative error using Eqn. 3.27 for an LD function space because the difference between two LD approximations is itself a piecewise-linear function. For a linear function within a cell, the maximum magnitude of that function must occur at the edges.

The situation is not so simple for the L^2 norm, defined as

$$\|u\|_{L^2} = \sqrt{\int_{x_L}^{x_R} |u(x)|^2 \, dx}. \tag{B.1}$$

If $\tilde{\phi}_1$ and $\tilde{\phi}_2$ are LD functions within a cell, let $\Delta\phi_L = \tilde{\phi}_1(x_L) - \tilde{\phi}_2(x_L)$ and $\Delta\phi_R = \tilde{\phi}_1(x_R) - \tilde{\phi}_2(x_R)$.

To compute the integral of the L_2 norm over one cell, consider a function $\Delta\phi(x) = \tilde{\phi}_1(x) - \tilde{\phi}_2(x)$. $\Delta\phi(x)$ must itself be a linear function. Choosing $x_L = 0$ and $x_R = h$ for simplicity, $\Delta\phi(x)$ can be represented as a generic linear function in cell i of width h_i.

$$\Delta\phi_i(x) = \frac{\Delta\phi_{i,R} - \Delta\phi_{i,L}}{h_i} x + \Delta\phi_{i,L} \tag{B.2}$$

Substituting into Eqn. B.1, the square of the L^2 norm over a cell is

$$\begin{aligned} \|\Delta\phi_i(x)\|_{L^2}^2 &= \int_0^{h_i} \left(\frac{\Delta\phi_{i,R} - \Delta\phi_{i,L}}{h_i} x + \Delta\phi_{i,L} \right)^2 dx \\ &= \left[\frac{(\Delta\phi_{i,R} - \Delta\phi_{i,L})^2}{3} + \Delta\phi_{i,L}\Delta\phi_{i,R} \right] h_i. \end{aligned} \tag{B.3}$$

Expanding the integral over all cells and using substituting into Eqn. B.1, the L_2 norm of $\Delta\phi(x)$

over the spatial domain of N cells is given by

$$\|\Delta\phi(x)\|_{L^2} = \sqrt{\sum_{i=1}^{N} \left[\frac{(\Delta\phi_{i,R} - \Delta\phi_{i,L})^2}{3} + \Delta\phi_{i,L}\Delta\phi_{i,R} \right] h_i}. \tag{B.4}$$

APPENDIX C

FOURIER ANALYSIS

Fourier analysis is utilized as a semi-analytic method to evaluate the convergence ratio of selected S_2, constant-solution problems. It is not fully analytic because the slowest-damping error mode λ is determined numerically. In particular, a problem of this class is modeled as a two-grid, two-cell problem in which a left boundary source condition and a right boundary reflective condition are prescribed to achieve a constant solution ϕ for a two-region problem. This problem of a finite-thickness slab with boundary conditions is equivalent to the infinite-thickness slab problem in which the region pair from the finite-width problem is periodic in x in both directions.

The error in $\phi^{\pm,(\ell)}$ at the cell edges, $\delta\phi^{\pm,(\ell)}$, can be conceived as a superposition of Fourier modes, where

$$\delta\phi^{\pm,(\ell)}(x_{i+\frac{1}{2}}) = \phi^{\pm}_{\mathrm{ICS}}(x_{i+\frac{1}{2}}) - \phi^{\pm,(\ell)}_{i+\frac{1}{2}} = \int_0^{2\pi} \epsilon^{\pm,(\ell)}(\lambda) e^{j\lambda x_{i+\frac{1}{2}}}\, d\lambda. \tag{C.1}$$

C.1 S_2 Moment Equations for the Fourier-Mode Error

To characterize the error in the two-cell, two-grid, finite slab problem, we substitute ϕ_{ICS} for ϕ in each of the S_2 moment Eqns. 2.2-2.5. Similarly, we substitute iterates $\phi^{\pm,(\ell+\frac{1}{2})}$ and $\phi^{\pm,(\ell)}$ into the left-hand-sides and right-hand-sides, respectively of these equations. Then, each equation with the ϕ iterates is subtracted from its counterpart with $\phi = \phi_{\mathrm{ICS}}$. Hence, each occurrence of $\phi^{(\ell)}$ and $\phi^{(\ell+\frac{1}{2})}$ in the S_2 moment equations is replaced with $\delta\phi^{(\ell)}$ and $\delta\phi^{(\ell+\frac{1}{2})}$, respectively. For $\mu > 0$, B_L,

$$\begin{aligned}
& \frac{1}{2}\left(\langle\mu^+_{i,L}\rangle\delta\phi^{+,(\ell+\frac{1}{2})}_{i,L} + \langle\mu^+_{i,R}\rangle\delta\phi^{+,(\ell+\frac{1}{2})}_{i,R}\right) - \langle\mu^+_{i-1,R}\rangle\delta\phi^{+,(\ell+\frac{1}{2})}_{i-1,R} \\
+ \quad & \frac{1}{2}\sigma_{t,i}h_i\left(\frac{2}{3}\delta\phi^{+,(\ell+\frac{1}{2})}_{i,L} + \frac{1}{3}\delta\phi^{+,(\ell+\frac{1}{2})}_{i,R}\right) \\
= \quad & \frac{1}{2}\sigma_{s,i}h_i\left[\frac{1}{3}\left(\delta\phi^{+,(\ell)}_{i,L} + \delta\phi^{-,(\ell)}_{i,L}\right) + \frac{1}{6}\left(\delta\phi^{+,(\ell)}_{i,R} + \delta\phi^{-,(\ell)}_{i,R}\right)\right].
\end{aligned} \tag{C.2}$$

For $\mu > 0$, B_R,

$$\begin{aligned} & \frac{1}{2}\left(\langle\mu_{i,R}^{+}\rangle\delta\phi_{i,R}^{+,(\ell+\frac{1}{2})} - \langle\mu_{i,L}^{+}\rangle\delta\phi_{i,L}^{+,(\ell+\frac{1}{2})}\right) \\ + \quad & \frac{1}{2}\sigma_{t,i}h_i\left(\frac{1}{3}\delta\phi_{i,L}^{+,(\ell+\frac{1}{2})} + \frac{2}{3}\delta\phi_{i,R}^{+,(\ell+\frac{1}{2})}\right) \\ = \quad & \frac{1}{2}\sigma_{s,i}h_i\left[\frac{1}{6}\left(\delta\phi_{i,L}^{+,(\ell)} + \delta\phi_{i,L}^{-,(\ell)}\right) + \frac{1}{3}\left(\delta\phi_{i,R}^{+,(\ell)} + \delta\phi_{i,R}^{-,(\ell)}\right)\right]. \end{aligned} \tag{C.3}$$

For $\mu < 0$, B_L,

$$\begin{aligned} & \frac{1}{2}\left(\langle\mu_{i,R}^{-}\rangle\delta\phi_{i,R}^{-,(\ell+\frac{1}{2})} - \langle\mu_{i,L}^{-}\rangle\delta\phi_{i,L}^{-,(\ell+\frac{1}{2})}\right) \\ + \quad & \frac{1}{2}\sigma_{t,i}h_i\left(\frac{2}{3}\delta\phi_{i,L}^{-,(\ell+\frac{1}{2})} + \frac{1}{3}\delta\phi_{i,R}^{-,(\ell+\frac{1}{2})}\right) \\ = \quad & \frac{1}{2}\sigma_{s,i}h_i\left[\frac{1}{3}\left(\delta\phi_{i,L}^{+,(\ell)} + \delta\phi_{i,L}^{-,(\ell)}\right) + \frac{1}{6}\left(\delta\phi_{i,R}^{+,(\ell)} + \delta\phi_{i,R}^{-,(\ell)}\right)\right]. \end{aligned} \tag{C.4}$$

For $\mu < 0$, B_R,

$$\begin{aligned} & -\frac{1}{2}\left(\langle\mu_{i,L}^{-}\rangle\delta\phi_{i,L}^{-,(\ell+\frac{1}{2})} + \langle\mu_{i,R}^{-}\rangle\delta\phi_{i,R}^{-,(\ell+\frac{1}{2})}\right) + \langle\mu_{i+1,L}^{-}\rangle\delta\phi_{i+1,L}^{-,(\ell+\frac{1}{2})} \\ + \quad & \frac{1}{2}\sigma_{t,i}h_i\left(\frac{1}{3}\delta\phi_{i,L}^{-,(\ell+\frac{1}{2})} + \frac{2}{3}\delta\phi_{i,R}^{-,(\ell+\frac{1}{2})}\right) \\ = \quad & \frac{1}{2}\sigma_{s,i}h_i\left[\frac{1}{6}\left(\delta\phi_{i,L}^{+,(\ell)} + \delta\phi_{i,L}^{-,(\ell)}\right) + \frac{1}{3}\left(\delta\phi_{i,R}^{+,(\ell)} + \delta\phi_{i,R}^{-,(\ell)}\right)\right]. \end{aligned} \tag{C.5}$$

We make two modifications to Eqns. C.2-C.5. Since this analysis is in S_2, the $\langle\mu^{\pm}\rangle$ parameters are known constants. Therefore, to simplify the notation, each $\langle\mu^{+}\rangle$ is replaced with $\hat{\mu}$, and each $\langle\mu^{-}\rangle$ is replaced with $-\hat{\mu}$, where $\hat{\mu} = \frac{1}{\sqrt{3}}$, the magnitude of the Gauss quadrature points used in S_2.

To obtain a spectral radius for convergence, the maximum eigenvalue is computed for each of a predefined number of evenly-spaced λ values, where $\lambda \in [0, 2\pi)$. The maximum overall eigenvalue is then taken to be the spectral radius. The half-range flux error $\delta\phi^{\pm}(x, \lambda)$ for a single

Fourier mode λ can be expressed as

$$\delta\phi^{\pm}(x,\lambda) = \epsilon^{\pm}_{\lambda}(x)e^{j\lambda x}, \tag{C.6}$$

where $\epsilon^{\pm}_{\lambda}(x)$ is the Fourier coefficient at a particular edge x. To simplify the notation $\epsilon^{\pm}$ and $\delta\phi^{\pm}$ are assumed to be specific to the chosen λ:

$$\delta\phi^{\pm} = \epsilon^{\pm}e^{j\lambda x}. \tag{C.7}$$

Substituting Eqn. C.7 into Eqns. C.2-C.5, the resulting S_2 single-mode Fourier error equations are, for $\mu > 0$, B_L,

$$\begin{aligned}
& \frac{1}{2}\left(\langle\mu^{+}_{i,L}\rangle\epsilon^{+,(\ell+\frac{1}{2})}_{i,L}e^{j\lambda x_{i-\frac{1}{2}}} + \langle\mu^{+}_{i,R}\rangle\epsilon^{+,(\ell+\frac{1}{2})}_{i,R}e^{j\lambda x_{i+\frac{1}{2}}}\right) - \langle\mu^{+}_{i-1,R}\rangle\epsilon^{+,(\ell+\frac{1}{2})}_{i-1,R}e^{j\lambda x_{i-\frac{1}{2}}} \\
+ \quad & \frac{1}{2}\sigma_{t,i}h_i\left(\frac{2}{3}\epsilon^{+,(\ell+\frac{1}{2})}_{i,L}e^{j\lambda x_{i-\frac{1}{2}}} + \frac{1}{3}\epsilon^{+,(\ell+\frac{1}{2})}_{i,R}e^{j\lambda x_{i+\frac{1}{2}}}\right) \\
= \quad & \frac{1}{2}\sigma_{s,i}h_i\left[\frac{1}{3}\left(\epsilon^{+,(\ell)}_{i,L}e^{j\lambda x_{i-\frac{1}{2}}} + \epsilon^{-,(\ell)}_{i,L}e^{j\lambda x_{i-\frac{1}{2}}}\right) + \frac{1}{6}\left(\epsilon^{+,(\ell)}_{i,R}e^{j\lambda x_{i+\frac{1}{2}}} + \epsilon^{-,(\ell)}_{i,R}e^{j\lambda x_{i+\frac{1}{2}}}\right)\right],
\end{aligned} \tag{C.8}$$

for $\mu > 0$, B_R,

$$\begin{aligned}
& \frac{1}{2}\left(\langle\mu^{+}_{i,R}\rangle\epsilon^{+,(\ell+\frac{1}{2})}_{i,R}e^{j\lambda x_{i+\frac{1}{2}}} - \langle\mu^{+}_{i,L}\rangle\epsilon^{+,(\ell+\frac{1}{2})}_{i,L}e^{j\lambda x_{i-\frac{1}{2}}}\right) \\
+ \quad & \frac{1}{2}\sigma_{t,i}h_i\left(\frac{1}{3}\epsilon^{+,(\ell+\frac{1}{2})}_{i,L}e^{j\lambda x_{i-\frac{1}{2}}} + \frac{2}{3}\epsilon^{+,(\ell+\frac{1}{2})}_{i,R}e^{j\lambda x_{i+\frac{1}{2}}}\right) \\
= \quad & \frac{1}{2}\sigma_{s,i}h_i\left[\frac{1}{6}\left(\epsilon^{+,(\ell)}_{i,L}e^{j\lambda x_{i-\frac{1}{2}}} + \epsilon^{-,(\ell)}_{i,L}e^{j\lambda x_{i-\frac{1}{2}}}\right) + \frac{1}{3}\left(\epsilon^{+,(\ell)}_{i,R}e^{j\lambda x_{i+\frac{1}{2}}} + \epsilon^{-,(\ell)}_{i,R}e^{j\lambda x_{i+\frac{1}{2}}}\right)\right],
\end{aligned} \tag{C.9}$$

for $\mu < 0$, B_L,

$$\begin{aligned}
& \frac{1}{2}\left(\langle\mu^{-}_{i,R}\rangle\epsilon^{-,(\ell+\frac{1}{2})}_{i,R}e^{j\lambda x_{i+\frac{1}{2}}} - \langle\mu^{-}_{i,L}\rangle\epsilon^{-,(\ell+\frac{1}{2})}_{i,L}e^{j\lambda x_{i-\frac{1}{2}}}\right) \\
+ \quad & \frac{1}{2}\sigma_{t,i}h_i\left(\frac{2}{3}\epsilon^{-,(\ell+\frac{1}{2})}_{i,L}e^{j\lambda x_{i-\frac{1}{2}}} + \frac{1}{3}\epsilon^{-,(\ell+\frac{1}{2})}_{i,R}e^{j\lambda x_{i+\frac{1}{2}}}\right) \\
= \quad & \frac{1}{2}\sigma_{s,i}h_i\left[\frac{1}{3}\left(\epsilon^{+,(\ell)}_{i,L}e^{j\lambda x_{i-\frac{1}{2}}} + \epsilon^{-,(\ell)}_{i,L}e^{j\lambda x_{i-\frac{1}{2}}}\right) + \frac{1}{6}\left(\epsilon^{+,(\ell)}_{i,R}e^{j\lambda x_{i+\frac{1}{2}}} + \epsilon^{-,(\ell)}_{i,R}e^{j\lambda x_{i+\frac{1}{2}}}\right)\right],
\end{aligned} \tag{C.10}$$

and for $\mu < 0$, B_R,

$$\begin{aligned} & -\frac{1}{2}\left(\langle\mu_{i,L}^{-}\rangle\epsilon_{i,L}^{-,(\ell+\frac{1}{2})}e^{j\lambda x_{i-\frac{1}{2}}} + \langle\mu_{i,R}^{-}\rangle\epsilon_{i,R}^{-,(\ell+\frac{1}{2})}e^{j\lambda x_{i+\frac{1}{2}}}\right) + \langle\mu_{i+1,L}^{-}\rangle\epsilon_{i+1,L}^{-,(\ell+\frac{1}{2})}e^{j\lambda x_{i+\frac{1}{2}}} \\ + \quad & \frac{1}{2}\sigma_{t,i}h_i\left(\frac{1}{3}\epsilon_{i,L}^{-,(\ell+\frac{1}{2})}e^{j\lambda x_{i-\frac{1}{2}}} + \frac{2}{3}\epsilon_{i,R}^{-,(\ell+\frac{1}{2})}e^{j\lambda x_{i+\frac{1}{2}}}\right) \\ = \quad & \frac{1}{2}\sigma_{s,i}h_i\left[\frac{1}{6}\left(\epsilon_{i,L}^{+,(\ell)}e^{j\lambda x_{i-\frac{1}{2}}} + \epsilon_{i,L}^{-,(\ell)}e^{j\lambda x_{i-\frac{1}{2}}}\right) + \frac{1}{3}\left(\epsilon_{i,R}^{+,(\ell)}e^{j\lambda x_{i+\frac{1}{2}}} + \epsilon_{i,R}^{-,(\ell)}e^{j\lambda x_{i+\frac{1}{2}}}\right)\right] \end{aligned} \tag{C.11}$$

We now have S_2 moment equations for the Fourier error coefficients $\bar{\epsilon}^{(\ell)}$ and $\bar{\epsilon}^{(\ell+\frac{1}{2})}$. The next step is to adapt the form of the single-cell system of Eqns. C.8-C.11 to another form depicting a two-cell system. Equations C.8-C.11 are applied to the left cell by substituting $i = 1$ and to the right cell by substituting $i = 2$, resulting in a system of eight equations and eight unknowns.

C.2 Determination of Fourier Coefficients

C.2.1 Source Iteration

Equations C.8-C.11 form the system characterizing one SI sweep in one cell. An 8×8 system must be constructed to characterize one SI sweep across the 2-cell fine grid. Redefining this 4×4 single-cell system as an 8×8 two-cell system, the 8×8 system models source iteration as follows:

$$\mathbf{A}\bar{\epsilon}^{(\ell+\frac{1}{2})} = \mathbf{B}\bar{\epsilon}^{(\ell)}. \tag{C.12}$$

Using the row order of Table 3.2 and the column order of Table 3.3, we construct $\vec{\epsilon}$, $\mathbf{A}$, and $\mathbf{B}$.

$$\vec{\epsilon} = \begin{bmatrix} \epsilon_{i,L}^{-} & \epsilon_{i,R}^{-} & \epsilon_{i,L}^{+} & \epsilon_{i,R}^{+} & \epsilon_{i+1,L}^{-} & \epsilon_{i+1,R}^{-} & \epsilon_{i+1,L}^{+} & \epsilon_{i+1,R}^{+} \end{bmatrix}^T \tag{C.13}$$

To construct $\mathbf{A}$ and $\mathbf{B}$, we look to Eqns. C.8-C.11. In addition to populating the matrices for two adjacent cells, we divide both by $e^{j\lambda x_{i-\frac{1}{2}}}$ in order to simplify some elements.

$$\mathbf{A} = \begin{bmatrix} 0 & 0 & \left(\frac{\hat{\mu}}{2}+\frac{\sigma_{t,i}h_i}{3}\right) & \left(\frac{\hat{\mu}}{2}+\frac{\sigma_{t,i}h_i}{6}\right)e^{j\lambda h_i} \\ 0 & 0 & \left(-\frac{\hat{\mu}}{2}+\frac{\sigma_{t,i}h_i}{6}\right) & \left(\frac{\hat{\mu}}{2}+\frac{\sigma_{t,i}h_i}{3}\right)e^{j\lambda h_i} \\ \left(\frac{\hat{\mu}}{2}+\frac{\sigma_{t,i}h_i}{3}\right) & \left(-\frac{\hat{\mu}}{2}+\frac{\sigma_{t,i}h_i}{6}\right)e^{j\lambda h_i} & 0 & 0 \\ \left(\frac{\hat{\mu}}{2}+\frac{\sigma_{t,i}h_i}{6}\right) & \left(\frac{\hat{\mu}}{2}+\frac{\sigma_{t,i}h_i}{3}\right)e^{j\lambda h_i} & 0 & 0 \\ 0 & 0 & 0 & -\hat{\mu}e^{j\lambda h_i} \\ 0 & 0 & 0 & 0 \\ 0 & 0 & 0 & 0 \\ -\hat{\mu}e^{j\lambda(h_i+h_{i+1})} & 0 & 0 & 0 \end{bmatrix} \begin{matrix} 0 & 0 \\ 0 & 0 \\ 0 & 0 \\ -\hat{\mu}e^{j\lambda h_i} & 0 \\ 0 & 0 \\ 0 & 0 \\ \left(-\frac{\hat{\mu}}{2}+\frac{\sigma_{t,i+1}h_{i+1}}{3}\right)e^{j\lambda h_i} & \left(\frac{\hat{\mu}}{2}+\frac{\sigma_{t,i+1}h_{i+1}}{6}\right)e^{j\lambda(h_i+h_{i+1})} \\ \left(\frac{\hat{\mu}}{2}+\frac{\sigma_{t,i+1}h_{i+1}}{6}\right)e^{j\lambda h_i} & \left(\frac{\hat{\mu}}{2}+\frac{\sigma_{t,i+1}h_{i+1}}{3}\right)e^{j\lambda(h_i+h_{i+1})} \end{matrix} \begin{bmatrix} 0 & -\hat{\mu} \\ 0 & 0 \\ 0 & 0 \\ 0 & 0 \\ \left(\frac{\hat{\mu}}{2}+\frac{\sigma_{t,i+1}h_{i+1}}{3}\right)e^{j\lambda h_i} & \left(\frac{\hat{\mu}}{2}+\frac{\sigma_{t,i+1}h_{i+1}}{6}\right)e^{j\lambda(h_i+h_{i+1})} \\ \left(-\frac{\hat{\mu}}{2}+\frac{\sigma_{t,i+1}h_{i+1}}{6}\right)e^{j\lambda h_i} & \left(\frac{\hat{\mu}}{2}+\frac{\sigma_{t,i+1}h_{i+1}}{3}\right)e^{j\lambda(h_i+h_{i+1})} \\ 0 & 0 \\ 0 & 0 \end{bmatrix} \tag{C.14}$$

$$\mathbf{B} = \begin{bmatrix} \frac{\sigma_{s,i}h_i}{6} & \frac{\sigma_{s,i}h_i}{12}e^{j\lambda h_i} & \frac{\sigma_{s,i}h_i}{6} & \frac{\sigma_{s,i}h_i}{12}e^{j\lambda h_i} \\ \frac{\sigma_{s,i}h_i}{12} & \frac{\sigma_{s,i}h_i}{6}e^{j\lambda h_i} & \frac{\sigma_{s,i}h_i}{12} & \frac{\sigma_{s,i}h_i}{6}e^{j\lambda h_i} \\ \frac{\sigma_{s,i}h_i}{6} & \frac{\sigma_{s,i}h_i}{12}e^{j\lambda h_i} & \frac{\sigma_{s,i}h_i}{6} & \frac{\sigma_{s,i}h_i}{12}e^{j\lambda h_i} \\ \frac{\sigma_{s,i}h_i}{12} & \frac{\sigma_{s,i}h_i}{6}e^{j\lambda h_i} & \frac{\sigma_{s,i}h_i}{12} & \frac{\sigma_{s,i}h_i}{6}e^{j\lambda h_i} \\ 0 & 0 & 0 & 0 \\ 0 & 0 & 0 & 0 \\ 0 & 0 & 0 & 0 \\ 0 & 0 & 0 & 0 \end{bmatrix} \begin{bmatrix} 0 & 0 & 0 & 0 \\ 0 & 0 & 0 & 0 \\ 0 & 0 & 0 & 0 \\ 0 & 0 & 0 & 0 \\ \frac{\sigma_{s,i+1}h_{i+1}}{6}e^{j\lambda h_i} & \frac{\sigma_{s,i+1}h_{i+1}}{12}e^{j\lambda(h_i+h_{i+1})} & \frac{\sigma_{s,i+1}h_{i+1}}{6}e^{j\lambda h_i} & \frac{\sigma_{s,i+1}h_{i+1}}{12}e^{j\lambda(h_i+h_{i+1})} \\ \frac{\sigma_{s,i+1}h_{i+1}}{12}e^{j\lambda h_i} & \frac{\sigma_{s,i+1}h_{i+1}}{6}e^{j\lambda(h_i+h_{i+1})} & \frac{\sigma_{s,i+1}h_{i+1}}{12}e^{j\lambda h_i} & \frac{\sigma_{s,i+1}h_{i+1}}{6}e^{j\lambda(h_i+h_{i+1})} \\ \frac{\sigma_{s,i+1}h_{i+1}}{6}e^{j\lambda h_i} & \frac{\sigma_{s,i+1}h_{i+1}}{12}e^{j\lambda(h_i+h_{i+1})} & \frac{\sigma_{s,i+1}h_{i+1}}{6}e^{j\lambda h_i} & \frac{\sigma_{s,i+1}h_{i+1}}{12}e^{j\lambda(h_i+h_{i+1})} \\ \frac{\sigma_{s,i+1}h_{i+1}}{12}e^{j\lambda h_i} & \frac{\sigma_{s,i+1}h_{i+1}}{6}e^{j\lambda(h_i+h_{i+1})} & \frac{\sigma_{s,i+1}h_{i+1}}{12}e^{j\lambda h_i} & \frac{\sigma_{s,i+1}h_{i+1}}{6}e^{j\lambda(h_i+h_{i+1})} \end{bmatrix} \tag{C.15}$$

C.2.2 Multigrid Acceleration

So far, we've shown how to apply Fourier analysis to source iteration.

First, we consider how to solve for the coarse-grid error $\delta\vec{\psi}_C^{(\ell+1)}$. Applying Eqns. C.2-C.5 to a two-grid system and reexpressing in matrix form,

$$\mathbf{A}'\delta\vec{\psi}_C^{(\ell+\frac{1}{2})} = \mathbf{B}'\delta\vec{\psi}_C^{(\ell)}, \tag{C.16}$$

where $\mathbf{A}'$ represents the LHS coefficents of the system and $\mathbf{B}'$ the RHS coefficients.

Because $\delta\vec{\psi}_C^{(\ell+1)}$ applies to a 4×4 system, the 8×8 matrix $\mathbf{A}' - \mathbf{B}'$ must be reduced to a 4×4

matrix to perform the coarse-grid matrix solve.

The row reduction described by Eqns. 3.10-3.13 can be performed using matrix multiplication. This transformation is achieved by multiplying $\mathbf{R}$,

$$\mathbf{R} = \begin{bmatrix} 1 & \frac{h_{i+1}}{h_i+h_{i+1}} & 0 & 0 & \frac{h_{i+1}}{h_i+h_{i+1}} & 0 & 0 & 0 \\ 0 & 0 & 1 & \frac{h_{i+1}}{h_i+h_{i+1}} & 0 & 0 & \frac{h_{i+1}}{h_i+h_{i+1}} & 0 \\ 0 & \frac{h_i}{h_i+h_{i+1}} & 0 & 0 & \frac{h_i}{h_i+h_{i+1}} & 1 & 0 & 0 \\ 0 & 0 & 0 & \frac{h_i}{h_i+h_{i+1}} & 0 & 0 & \frac{h_i}{h_i+h_{i+1}} & 1 \end{bmatrix}, \tag{C.17}$$

by the matrix $\mathbf{A}' - \mathbf{B}'$ describing the fine-cell-pair 8×8 system. Next, the row-reduced 4×8 matrix is then multiplied by matrix $\mathbf{G}'$, which consolidates the columns according to the linearized scheme. Here,

$$\mathbf{G}' = \begin{bmatrix} 1 & 0 & 0 & 0 \\ \frac{1}{2} & \frac{1}{2} & 0 & 0 \\ 0 & 0 & 1 & 0 \\ 0 & 0 & \frac{1}{2} & \frac{1}{2} \\ \frac{1}{2} & \frac{1}{2} & 0 & 0 \\ 0 & 1 & 0 & 0 \\ 0 & 0 & \frac{1}{2} & \frac{1}{2} \\ 0 & 0 & 0 & 1 \end{bmatrix}. \tag{C.18}$$

Then, $\delta\vec{\psi}_C^{(\ell+1)}$ is defined as satisfying the equation

$$\mathbf{R}(\mathbf{A}' - \mathbf{B}')\mathbf{G}'\delta\vec{\psi}_C^{(\ell+1)} = \vec{0}. \tag{C.19}$$

If we note that the expanded and linearly-interpolated fine-grid error $\delta\vec{\psi}^{(\ell+1)}$ is given as

$$\delta\vec{\psi}^{(\ell+1)} = \mathbf{G}'\delta\vec{\psi}_C^{(\ell+1)}, \tag{C.20}$$

Eqn. C.19 can be reexpressed in terms of $\delta\vec{\psi}^{(\ell+1)}$.

$$\mathbf{R}(\mathbf{A}' - \mathbf{B}')\delta\vec{\psi}^{(\ell+1)} = \vec{0}. \tag{C.21}$$

The identity given in Eqn. C.21 will prove useful later.

In combining two cells into one, we consider how the inner-edge values are interpolated onto the fine grid. In the case of $\psi_{i,R}^{(\ell+1)}$:

$$\psi_{i,R}^{(\ell+1)} = \frac{1}{2}(\psi_{i,L}^{(\ell+1)} + \psi_{i+1,R}^{(\ell+1)})\gamma_{i,R}^{(\ell+\frac{1}{2})}, \tag{C.22}$$

where

$$\gamma_{i,R}^{(\ell+\frac{1}{2})} = \frac{2\psi_{i,R}^{(\ell+\frac{1}{2})}}{\psi_{i,L}^{(\ell+\frac{1}{2})} + \psi_{i+1,R}^{(\ell+\frac{1}{2})}}. \tag{C.23}$$

Equation C.22 expresses $\psi_{i,R}^{(\ell+1)}$ in terms of a γ multiplicative correction. To transform it into a form suitable for Fourier analysis, it is reexpressed in terms of an additive correction. For a constant-solution problem, the iterate $\psi^{(\ell+1)}$ can be expressed as the sum of the exact solution ψ_{EAS} and the error $\delta\psi^{(\ell+1)}$.

$$\psi^{(\ell+1)} = \psi_{\mathrm{EAS}} + \delta\psi^{(\ell+1)}. \tag{C.24}$$

Substituting from Eqn. C.24 for the outer-edge ψ iterates and from Eqn. C.23 for $\gamma_{i,R}^{(\ell+\frac{1}{2})}$ into Eqn. C.22,

$$\psi_{i,R}^{(\ell+1)} = \frac{\left(2\psi_{\mathrm{EAS}} + \delta\psi_{i,L}^{(\ell+1)} + \delta\psi_{i+1,R}^{(\ell+1)}\right)\left(\psi_{\mathrm{EAS}} + \delta\psi_{i,R}^{(\ell+\frac{1}{2})}\right)}{2\psi_{\mathrm{EAS}} + \delta\psi_{i,L}^{(\ell+\frac{1}{2})} + \delta\psi_{i+1,R}^{(\ell+\frac{1}{2})}}. \tag{C.25}$$

Multiplying the numerator and denominator by $2\psi_{\mathrm{EAS}} - (\delta\psi_{i,L}^{(\ell+\frac{1}{2})} + \delta\psi_{i+1,R}^{(\ell+\frac{1}{2})})$,

$$\psi_{i,R}^{(\ell+1)} = \frac{\left(2\psi_{\mathrm{EAS}} + \delta\psi_{i,L}^{(\ell+1)} + \delta\psi_{i+1,R}^{(\ell+1)}\right)\left(\psi_{\mathrm{EAS}} + \delta\psi_{i,R}^{(\ell+\frac{1}{2})}\right)\left(2\psi_{\mathrm{EAS}} - \left(\delta\psi_{i,L}^{(\ell+\frac{1}{2})} + \delta\psi_{i+1,R}^{(\ell+\frac{1}{2})}\right)\right)}{\left(2\psi_{\mathrm{EAS}}\right)^2 - \left(\delta\psi_{i,L}^{(\ell+\frac{1}{2})} + \delta\psi_{i+1,R}^{(\ell+\frac{1}{2})}\right)^2}. \tag{C.26}$$

Assuming the $\delta\psi$ errors are small compared to the constant solution, the denominator can be sim-

plified to $4\psi_{\mathrm{EAS}}^2$. Furthermore, terms in the numerator on the order of $(\delta\psi)^2$ are eliminated, leaving,

$$\psi_{i,R}^{(\ell+1)} \approx \psi_{\mathrm{EAS}} + \frac{1}{2}\left(\sigma\psi_{i,L}^{(\ell+1)} + \delta\psi_{i+1,R}^{(\ell+1)}\right) + \delta\psi_{i,R}^{(\ell+\frac{1}{2})} - \frac{1}{2}\left(\sigma\psi_{i,L}^{(\ell+\frac{1}{2})} + \delta\psi_{i+1,R}^{(\ell+\frac{1}{2})}\right). \tag{C.27}$$

Subtracting the exact solution from both sides,

$$\delta\psi_{i,R}^{(\ell+1)} \approx \frac{1}{2}\left(\delta\psi_{i,L}^{(\ell+1)} + \delta\psi_{i+1,R}^{(\ell+1)}\right) + \delta\psi_{i,R}^{(\ell+\frac{1}{2})} - \frac{1}{2}\left(\delta\psi_{i,L}^{(\ell+\frac{1}{2})} + \delta\psi_{i+1,R}^{(\ell+\frac{1}{2})}\right). \tag{C.28}$$

Equation C.28 provides the needed linear relation between the $\delta\psi_{i,R}^{(\ell+1)}$ interpolated onto the fine grid and the iterates on which it depends. The same principle applies to $\delta\psi_{i+1,L}^{(\ell+1)}$. Replacing the S_N $\delta\psi_{i,R}^{(\ell+1)}$ and $\delta\psi_{i+1,L}^{(\ell+1)}$ with their S_2 counterparts,

$$\delta\phi_{i,R}^{\pm,(\ell+1)} \approx \frac{1}{2}\left(\delta\phi_{i,L}^{\pm,(\ell+1)} + \delta\phi_{i+1,R}^{\pm,(\ell+1)}\right) + \delta\phi_{i,R}^{\pm,(\ell+\frac{1}{2})} - \frac{1}{2}\left(\delta\phi_{i,L}^{\pm,(\ell+\frac{1}{2})} + \delta\phi_{i+1,R}^{\pm,(\ell+\frac{1}{2})}\right), \tag{C.29}$$

and

$$\delta\phi_{i+1,L}^{\pm,(\ell+1)} \approx \frac{1}{2}\left(\delta\phi_{i,L}^{\pm,(\ell+1)} + \delta\phi_{i+1,R}^{\pm,(\ell+1)}\right) + \delta\phi_{i+1,L}^{\pm,(\ell+\frac{1}{2})} - \frac{1}{2}\left(\delta\phi_{i,L}^{\pm,(\ell+\frac{1}{2})} + \delta\phi_{i+1,R}^{\pm,(\ell+\frac{1}{2})}\right). \tag{C.30}$$

The values $\delta\phi^{\pm,(\ell+1)}$ are given by

$$\delta\phi_{i,L}^{-,(\ell+1)} = \delta\phi_{i,L}^{-,(\ell+1)} \tag{C.31}$$

$$\delta\phi_{i,R}^{-,(\ell+1)} = \underbrace{\frac{\delta\phi_{i,L}^{-,(\ell+1)} + \delta\phi_{i+1,R}^{-,(\ell+1)}}{2}}_{\ell+1} + \underbrace{\delta\phi_{i,R}^{-,(\ell+\frac{1}{2})} - \frac{\delta\phi_{i,L}^{-,(\ell+\frac{1}{2})} + \delta\phi_{i+1,R}^{-,(\ell+\frac{1}{2})}}{2}}_{\ell+\frac{1}{2}} \tag{C.32}$$

$$\delta\phi_{i,L}^{+,(\ell+1)} = \delta\phi_{i,L}^{+,(\ell+1)} \tag{C.33}$$

$$\delta\phi_{i,R}^{+,(\ell+1)} = \underbrace{\frac{\delta\phi_{i,L}^{+,(\ell+1)} + \delta\phi_{i+1,R}^{+,(\ell+1)}}{2}}_{\ell+1} + \underbrace{\delta\phi_{i,R}^{+,(\ell+\frac{1}{2})} - \frac{\delta\phi_{i,L}^{+,(\ell+\frac{1}{2})} + \delta\phi_{i+1,R}^{+,(\ell+\frac{1}{2})}}{2}}_{\ell+\frac{1}{2}} \tag{C.34}$$

$$\delta\phi_{i+1,L}^{-,(\ell+1)} = \overbrace{\frac{\delta\phi_{i,L}^{-,(\ell+1)} + \delta\phi_{i+1,R}^{-,(\ell+1)}}{2}} + \overbrace{\delta\phi_{i+1,L}^{-,(\ell+\frac{1}{2})} - \frac{\delta\phi_{i,L}^{-,(\ell+\frac{1}{2})} + \delta\phi_{i+1,R}^{-,(\ell+\frac{1}{2})}}{2}} \tag{C.35}$$

$$\delta\phi_{i+1,R}^{-,(\ell+1)} = \delta\phi_{i+1,R}^{-,(\ell+1)} \tag{C.36}$$

$$\delta\phi_{i+1,L}^{+,(\ell+1)} = \underbrace{\frac{\delta\phi_{i,L}^{+,(\ell+1)} + \delta\phi_{i+1,R}^{+,(\ell+1)}}{2}}_{\ell+1} + \underbrace{\delta\phi_{i+1,L}^{+,(\ell+\frac{1}{2})} - \frac{\delta\phi_{i,L}^{+,(\ell+\frac{1}{2})} + \delta\phi_{i+1,R}^{+,(\ell+\frac{1}{2})}}{2}}_{\ell+\frac{1}{2}} \tag{C.37}$$

$$\delta\phi_{i+1,R}^{+,(\ell+1)} = \delta\phi_{i+1,R}^{+,(\ell+1)} \tag{C.38}$$

The updated coarse-grid parameters map directly to the corresponding fine-grid parameters. The inner-edge fine-grid parameters are updated from their values from the fine-grid sweep, the updated coarse-grid values, and the post-sweep, pre-coarse-matrix-solve coarse-grid values. The updated solution after one complete iterate given in Eqns. C.31-C.38 can be expressed more succinctly as a matrix equation:

$$\delta\vec{\phi}^{(\ell+1)} = \mathbf{C}'\delta\vec{\phi}_{C,8}^{(\ell+1)} + \mathbf{D}'\delta\vec{\phi}^{(\ell+\frac{1}{2})}, \tag{C.39}$$

where $\delta\vec{\phi}_{C,8}^{(\ell+1)}$ represents the $\delta\vec{\phi}_{C}^{(\ell+1)}$ error of the 4×4 system expanded for the 8×8 system, with zero-entries for the inner-edge parameters. A matrix $\mathbf{F}$ may be created which, when multiplied by $\delta\vec{\phi}_{C}^{(\ell+1)}$, maps the coarse-grid solution to the fine grid:

$$\delta\vec{\phi}_{C,8}^{(\ell+1)} = \mathbf{F}\delta\vec{\phi}_{C}^{(\ell+1)} \tag{C.40}$$

Here,

$$\mathbf{F} = \left[\begin{array}{cccc} 1 & 0 & 0 & 0 \\ 0 & 0 & 0 & 0 \\ 0 & 0 & 1 & 0 \\ 0 & 0 & 0 & 0 \\ 0 & 0 & 0 & 0 \\ \hline 0 & 1 & 0 & 0 \\ 0 & 0 & 0 & 0 \\ \hline 0 & 0 & 0 & 1 \end{array}\right]. \tag{C.41}$$

Recalling Eqn. C.21, multiplying Eqn. C.39 by $\mathbf{R}(\mathbf{A}' - \mathbf{B}')$ results in

$$\vec{0} = \mathbf{R}(\mathbf{A}' - \mathbf{B}')\delta\vec{\phi}^{(\ell+1)} = \mathbf{R}(\mathbf{A}' - \mathbf{B}')\left[\mathbf{C}'\delta\vec{\phi}_{C,8}^{(\ell+1)} + \mathbf{D}'\delta\vec{\phi}^{(\ell+\frac{1}{2})}\right], \tag{C.42}$$

or

$$\mathbf{R}(\mathbf{A}' - \mathbf{B}')\mathbf{C}'\delta\vec{\phi}_{C,8}^{(\ell+1)} = -\mathbf{R}(\mathbf{A}' - \mathbf{B}')\mathbf{D}'\delta\vec{\phi}^{(\ell+\frac{1}{2})}. \tag{C.43}$$

Substituting Eqn. C.40 into Eqn. C.43

$$\mathbf{R}(\mathbf{A}' - \mathbf{B}')\mathbf{C}'\mathbf{F}\delta\vec{\phi}_{C}^{(\ell+1)} = -\mathbf{R}(\mathbf{A}' - \mathbf{B}')\mathbf{D}'\delta\vec{\phi}^{(\ell+\frac{1}{2})}. \tag{C.44}$$

Then, expressing $\delta\vec{\phi}_{C}^{(\ell+1)}$ as a function of $\delta\vec{\phi}^{(\ell+\frac{1}{2})}$:

$$\delta\vec{\phi}_{C}^{(\ell+1)} = -[\mathbf{R}(\mathbf{A}' - \mathbf{B}')\mathbf{C}'\mathbf{F}]^{-1}\mathbf{R}(\mathbf{A}' - \mathbf{B}')\mathbf{D}'\delta\vec{\phi}^{(\ell+\frac{1}{2})}. \tag{C.45}$$

The coarse-grid iterate $\delta\vec{\phi}_{C}^{(\ell+1)}$ can now be used to apply the coarse-grid update the fine-grid iterate $\delta\vec{\phi}^{(\ell+1)}$. Comparing Eqn. C.20 and Eqns. C.31-C.38, it is seen that $\mathbf{G}' = \mathbf{C}'\mathbf{F}$.

Substituting Eqn. C.45 for $\delta\vec{\phi}_C^{(\ell+1)}$ in Eqn. C.40 and Eqn. C.40 in turn into Eqn. C.39

$$\begin{aligned}\delta\vec{\phi}^{(\ell+1)} &= -\mathbf{C}'\mathbf{F}[\mathbf{R}(\mathbf{A}'-\mathbf{B}')\mathbf{C}'\mathbf{F}]^{-1}\mathbf{R}(\mathbf{A}'-\mathbf{B}')\mathbf{D}'\delta\vec{\phi}^{(\ell+\frac{1}{2})} + \mathbf{D}'\delta\vec{\phi}^{(\ell+\frac{1}{2})} \\ &= \left[-\mathbf{C}'\mathbf{F}[\mathbf{R}(\mathbf{A}'-\mathbf{B}')\mathbf{C}'\mathbf{F}]^{-1}\mathbf{R}(\mathbf{A}'-\mathbf{B}')\mathbf{D}' + \mathbf{D}'\right]\delta\vec{\phi}^{(\ell+\frac{1}{2})}, \qquad \text{(C.46)}\end{aligned}$$

leading the following matrix equation describing one complete V-cycle on a two-grid, constant-solution system:

$$\delta\vec{\phi}^{(\ell+1)} = \left[-\mathbf{C}'\mathbf{F}[\mathbf{R}(\mathbf{A}'-\mathbf{B}')\mathbf{C}'\mathbf{F}]^{-1}\mathbf{R}(\mathbf{A}'-\mathbf{B}')\mathbf{D}' + \mathbf{D}'\right](\mathbf{A}')^{-1}\mathbf{B}'\delta\vec{\phi}^{(\ell)}. \qquad \text{(C.47)}$$

C.2.3 Transition to Fourier Domain

Modifications must be made to several matrices in order to adapt Eqn. C.47 for Fourier analysis. Matrices $\mathbf{F}$ and $\mathbf{R}$ are merely for collapsing columns and rows, respectively, and are not modified. The other matrices in Eqn. C.47, denoted by the prime ($\prime$) symbol, must be replaced with their Fourier equivalents. $\mathbf{A}$ and $\mathbf{B}$ have been computed from the previous discussion on source iteration (Eqns. C.14 and C.15).

As before for $\mathbf{C}'$ and $\mathbf{D}'$, we turn to Eqns. C.31-C.38 for $\mathbf{C}$ and $\mathbf{D}$. Each row corresponds to a parameter at $\ell+1$. Each column corresponds to a parameter at $\ell+\frac{1}{2}$. Hence, each row defines an element of $\delta\vec{\phi}^{(\ell+1)}$ as a linear combination of elements of $\delta\vec{\phi}^{(\ell+\frac{1}{2})}$.

In transitioning from a system defined in terms of the LD parameters $\delta\vec{\phi}$ to one defined in terms of the Fourier parameters $\vec{\epsilon}$, it is necessary to multiply each non-zero coefficient of the system described in Eqns. C.31-C.38 by the phase difference between the row LD parameter and

the column LD parameter. We obtain

$$\mathbf{C} = \begin{bmatrix} 1 & 0 & 0 & 0 & 0 & 0 & 0 & 0 \\ \frac{1}{2}e^{-j\lambda h_i} & 0 & 0 & 0 & 0 & \frac{1}{2}e^{j\lambda h_{i+1}} & 0 & 0 \\ 0 & 0 & 1 & 0 & 0 & 0 & 0 & 0 \\ 0 & 0 & \frac{1}{2}e^{-j\lambda h_i} & 0 & 0 & 0 & 0 & \frac{1}{2}e^{j\lambda h_{i+1}} \\ \frac{1}{2}e^{-j\lambda h_i} & 0 & 0 & 0 & 0 & \frac{1}{2}e^{j\lambda h_{i+1}} & 0 & 0 \\ 0 & 0 & 0 & 0 & 0 & 1 & 0 & 0 \\ 0 & 0 & \frac{1}{2}e^{-j\lambda h_i} & 0 & 0 & 0 & 0 & \frac{1}{2}e^{j\lambda h_{i+1}} \\ 0 & 0 & 0 & 0 & 0 & 0 & 0 & 1 \end{bmatrix} \tag{C.48}$$

and

$$\mathbf{D} = \begin{bmatrix} 0 & 0 & 0 & 0 & 0 & 0 & 0 & 0 \\ -\frac{1}{2}e^{-j\lambda h_i} & 1 & 0 & 0 & 0 & -\frac{1}{2}e^{j\lambda h_{i+1}} & 0 & 0 \\ 0 & 0 & 0 & 0 & 0 & 0 & 0 & 0 \\ 0 & 0 & -\frac{1}{2}e^{-j\lambda h_i} & 1 & 0 & 0 & 0 & -\frac{1}{2}e^{j\lambda h_{i+1}} \\ -\frac{1}{2}e^{-j\lambda h_i} & 0 & 0 & 0 & 1 & -\frac{1}{2}e^{j\lambda h_{i+1}} & 0 & 0 \\ 0 & 0 & 0 & 0 & 0 & 0 & 0 & 0 \\ 0 & 0 & -\frac{1}{2}e^{-j\lambda h_i} & 0 & 0 & 0 & 1 & -\frac{1}{2}e^{j\lambda h_{i+1}} \\ 0 & 0 & 0 & 0 & 0 & 0 & 0 & 0 \end{bmatrix}. \tag{C.49}$$

Performing the substitutions of $\mathbf{A}$, $\mathbf{B}$, $\mathbf{C}$, $\mathbf{D}$, $\vec{\epsilon}^{(\ell)}$, and $\vec{\epsilon}^{(\ell+1)}$ into Eqn. C.47,

$$\vec{\epsilon}^{(\ell+1)} = \underbrace{\left[-\mathbf{CF}[\mathbf{R}(\mathbf{A}-\mathbf{B})\mathbf{CF}]^{-1}\mathbf{R}(\mathbf{A}-\mathbf{B})\mathbf{D}+\mathbf{D}\right]\mathbf{A}^{-1}\mathbf{B}}_{\text{Fourier coefficient matrix}}\vec{\epsilon}^{(\ell)}. \tag{C.50}$$

C.3 Fourier Spectral Radius

Computation the Fourier spectral radius consists of determining the eigenvalue with the maximum magnitude over a range of λ sufficiently wide to represent every Fourier mode at the cell

edges. Hence, we evaluate the Fourier coefficient matrix of Eqn. C.50 for a number of evenly-spaced λ values in $[0, 2\pi)$ and determine the maximum-magnitude eigenvalue for each λ to obtain the spectral radius.